

1 ~~Comparative assessment of TROPOMI and OMI formaldehyde~~
2 ~~observations against MAX-DOAS network column~~
3 ~~measurements.~~Comparative assessment of TROPOMI and OMI
4 formaldehyde observations and validation against MAX-DOAS
5 network column measurements

6 Isabelle De Smedt¹, Gaia Pinardi¹, Corinne Vigouroux¹, Steven Compernelle¹, Alkis Bais², Nuria
7 Benavent³, Folkert Boersma^{4,5}, Ka-Lok Chan⁶, Sebastian Donner⁷, Kai-Uwe Eichmann⁸, Pascal
8 Hedelt⁶, François Hendrick¹, Hitoshi Irie⁹, Vinod Kumar⁷, Jean-Christopher Lambert¹, Bavo
9 Langerock¹, Christophe Lerot¹, Cheng Liu¹⁰, Diego Loyola⁶, Ankie PETERS⁴, Andreas Richter⁸,
10 Claudia Rivera Cárdenas¹¹, Fabian Romahn⁶, Robert George Ryan^{12,13}, Vinayak Sinha¹⁴, Nicolas
11 Theys¹, Jonas Vlietinck¹, Thomas Wagner⁷, Ting Wang¹⁵, Huan Yu¹, Michel Van Roozendael¹.

12 Correspondence to: Isabelle De Smedt (isabelle.desmedt@aeronomie.be)

- 13 1. Royal Belgian Institute for Space Aeronomy (BIRA-IASB), Ringlaan 3, 1180 Uccle, Belgium.
14 2. Laboratory of Atmospheric Physics, Aristotle University of Thessaloniki (AUTH), Thessaloniki, Greece.
15 3. Department of Atmospheric Chemistry and Climate, Institute of Physical Chemistry Rocasolano (CSIC), Madrid,
16 Spain.
17 4. Royal Netherlands Meteorological Institute (KNMI), De Bilt, the Netherlands.
18 5. Meteorology and Air Quality group, Wageningen University, the Netherlands.
19 6. Institut für Methodik der Fernerkundung (IMF), Deutsches Zentrum für Luft und Raumfahrt (DLR),
20 Oberpfaffenhofen, Germany.
21 7. Max-Planck-Institut für Chemie (MPI-C), Mainz, Germany.
22 8. Institute of Environmental Physics, University of Bremen (IUP-B), Bremen, Germany.
23 9. Center for Environmental Remote Sensing, Chiba University (Chiba U), Chiba, Japan
24 10. Department of Precision Machinery and Precision Instrumentation, University of Science and Technology of
25 China, Hefei, China.
26 11. Centro de Ciencias de la Atmósfera, Universidad Nacional Autónoma de México (UNAM), Mexico City, Mexico
27 12. School of Earth Sciences, The University of Melbourne, Melbourne, Australia
28 13. ARC Centre of Excellence for Climate System Science, Sydney, Australia
29 14. Department of Earth and Environmental Sciences, Indian Institute of Science Education and Research (IISER),
30 Mohali, India
31 15. Institute of Atmospheric Physics, Chinese Academy of Sciences (CAS), Beijing, China
32

33 **Abstract.** The Tropospheric Monitoring Instrument (TROPOMI), launched in October 2017 on board the Sentinel-
34 5 Precursor (S5P) satellite, monitors the composition of the Earth's atmosphere at an unprecedented horizontal
35 resolution as fine as 3.5x5.5 km². This paper assesses the performances of the TROPOMI formaldehyde (HCHO)
36 operational product compared to its predecessor, the OMI HCHO QA4ECV product, at different spatial and temporal
37 scales. The parallel development of the two algorithms favored the consistency of the products, which facilitates the
38 production of long-term combined time series. The main difference between the two satellite products is related to the
39 use of different cloud algorithms, leading to a positive bias of OMI compared to TROPOMI of up to 30% in Tropical
40 regions. We show that after switching off the explicit correction for cloud effects, the two datasets come into an
41 excellent agreement. For medium to large HCHO vertical columns (larger than 5x10¹⁵ molec.cm⁻²) the median bias
42 between OMI and TROPOMI HCHO columns is not larger than 10% (<0.4x10¹⁵ molec.cm⁻²). For lower columns,

43 OMI observations present a remaining positive bias of about 20% ($<0.8 \times 10^{15}$ molec.cm⁻²) compared to TROPOMI in
44 mid-latitude regions. Here, we also use a global network of 18 MAX-DOAS instruments to validate both satellite
45 sensors for a large range of HCHO columns. This work complements the study by Vigouroux et al. (2020) where a
46 global FTIR network is used to validate the TROPOMI HCHO operational product. Consistent with the FTIR
47 validation study, we find that for elevated HCHO columns, TROPOMI data are systematically low (-25% for HCHO
48 columns larger than 8×10^{15} molec.cm⁻²), while no significant bias is found for medium range column values. We
49 further show that OMI and TROPOMI data present equivalent biases for large HCHO levels. However, TROPOMI
50 significantly improves the precision of the HCHO observations at short temporal scales, and for low HCHO columns.
51 We show that compared to OMI, the precision of the TROPOMI HCHO columns is improved by 25% for individual
52 pixels, and up to a factor of 3 when considering daily averages in 20km-radius circles. The validation precision
53 obtained with daily TROPOMI observations is comparable to the one obtained with monthly OMI observations. To
54 illustrate the improved performances of TROPOMI in capturing weak HCHO signals, we present clear detection of
55 HCHO column enhancements related to shipping emissions in the Indian Ocean. This is achieved by averaging data
56 over a much shorter period (3 months) than required with previous sensors (5 years), and opens new perspectives to
57 study shipping emissions of VOCs and related atmospheric chemical interactions.

58 1 Introduction

59 Satellite observations of tropospheric formaldehyde (HCHO) columns have been used for years to support air quality
60 and chemistry-climate related studies from the regional to the global scale. Formaldehyde is an intermediate gas in
61 almost all oxidation chains of non-methane volatile organic compounds (NMVOC), leading to the production of
62 carbon monoxide (CO), and eventually carbon dioxide (CO₂). NMVOCs are, together with nitrogen oxides (NO_x),
63 CO and methane (CH₄), among the most important precursors of tropospheric ozone. NMVOCs also produce
64 secondary organic aerosols and influence the concentrations of hydroxyl radical (OH), the main tropospheric oxidant.
65 The major HCHO source in the remote atmosphere is CH₄ oxidation. Over the continents, the oxidation of other
66 NMVOCs emitted from vegetation, fires, traffic and industrial sources results in important and localised enhancements
67 of the HCHO levels. Because of its short lifetime (of the order of a few hours), HCHO in the boundary layer can be
68 related to the release of a large number of short-lived volatile hydrocarbons. Furthermore, HCHO observations provide
69 information on the chemical oxidation processes in the atmosphere, including CO chemical production from CH₄ and
70 NMVOC, the oxidation of isoprene into HCHO, which allows quantification of midday OH (Wells et al., Nature,
71 2019), and the tropospheric ozone production regimes that depend on the HCHO to NO₂ ratios (Jin et al., 2020).

72 Satellite observations of formaldehyde columns in the troposphere have been extensively reported in the literature
73 from a number of nadir UV sensors, e.g.: Global Ozone Monitoring Experiment (GOME; Chance et al., 2000; Palmer
74 et al., 2001; De Smedt et al., 2008), SCanning Imaging Absorption spectroMeter for Atmospheric CHartographY
75 (SCIAMACHY; Wittrock et al., 2006; De Smedt et al., 2008; 2010), Ozone Monitoring Instrument (OMI; González
76 Abad et al., 2015; De Smedt et al., 2015; 2018; Kaiser et al. 2018; Levelt et al., 2018), Global Ozone Monitoring
77 Experiment-2 (GOME-2; De Smedt et al., 2012; 2015; Vrekoussis et al., 2010; Hewson et al., 2013; Hassinen et al.,
78 2016), and Ozone Mapping and Profiler Suite (OMPS; Li et al., 2015; González Abad et al., 2016). They are used in

Formatted: Not Superscript/ Subscript

79 many studies related to air quality and climate change (e.g. Stavrakou et al., 2014; 2015; 2016; 2018; Fortems-Cheiney
80 et al., 2012; Marais et al., 2012; Mahajan et al., 2015; Choi et al., 2015; Zhu et al., 2016; Chan Miller et al., 2017; Jin
81 et al., 2017; Barkley et al., 2017; Cao et al., 2018; Khan et al., 2018; Surl et al., 2018; Shen et al. 2019; Su et al.; 2019;
82 Zyrichidou et al., 2019; Jin et al., 2020; Souri et al., 2020; Wells et al., 2020; Franco et al., 2021; Opacka et al., 2021).
83 Launched on board of the European Copernicus Sentinel-5 Precursor (S5P) satellite on 13 October 2017, the
84 TROPospheric Monitoring Instrument (TROPOMI, Veefkind et al., 2012) is designed for the daily monitoring of the
85 troposphere at the global scale. Compared to its predecessor OMI, its spatial resolution is about 16 times better with
86 at least the same signal to noise ratio per ground pixel. The improved TROPOMI capabilities for the observation of
87 HCHO have been illustrated for the detection of fire plumes and their transport (Alvarado et al., 2020; Theys et al.
88 2020), and the detection of rapid changes in anthropogenic emissions related to the COVID crisis in China and India
89 (Levelt et al., 2021; Sun et al. 2021). The TROPOMI observations extend the historical time series of midday
90 observations performed using OMI. Both datasets are used in combination for long-term trend studies (Li et al., 2020).
91 It is therefore important to evaluate their level of agreement and to report on the best practices to combine datasets
92 from different sensors.

93 The TROPOMI vertical column product requirements specify a single measurement precision of 12×10^{15} molec.cm⁻²,
94 4×10^{15} molec.cm⁻² at 20km spatial resolution, and a systematic uncertainty lower than 40% -80% (ESA, 2014). The
95 Copernicus user requirements, primarily defined for NMVOC measurements, are more stringent. For the
96 environmental air quality theme, the required maximum uncertainty is defined as 60% or 1.3×10^{15} molec.cm⁻² (least
97 stringent), at the spatial resolution of 20km and with a revisit time of 2 hours. The space and time resolution are less
98 stringent for the climate theme (30% or 1.3×10^{15} molec.cm⁻², 50km, 3 days) (Bovensmann et al., 2011; Langen et al.,
99 2017).

100 Given these rather strict product requirements and the diversity of the NMVOC species, lifetimes and sources
101 (biogenic, biomass burning or anthropogenic), a validation approach addressing a large variety of conditions
102 worldwide (tropical, temperate and boreal forests, urban and sub-urban areas) is needed, as well as continuous
103 measurements in order to obtain good statistics and capture the seasonal variations. Vigouroux et al. (2020) validated
104 the operational TROPOMI HCHO product using a global network of Fourier Transform Infrared (FTIR) instruments.
105 The study concluded that overall the HCHO product fulfils the requirements of the TROPOMI mission. Compared to
106 the FTIR data, the TROPOMI HCHO columns present a negative bias over high emission-concentrations sites (-31%
107 for HCHO columns larger than 8×10^{15} molec.cm⁻²) and a positive bias for clean sites (+26% for HCHO columns lower
108 than 2.5×10^{15} molec.cm⁻²). Based on clean sites, an upper limit of 1.3×10^{15} molec.cm⁻² was estimated for the deviation
109 of daily observations at a spatial resolution of 20km. It was also pointed out that this level of random uncertainty,
110 although reaching the Copernicus user requirements, is about twice as large as the expected theoretical noise
111 (individual pixel precision divided by the square root of the number of observations). However, Vigouroux et al.
112 (2020) do not address the consistency of TROPOMI HCHO with other satellite products and MAX-DOAS HCHO
113 observations.

114 The present paper is a follow-up of De Smedt et al. (2018), where the HCHO retrieval algorithm applied to both OMI
115 and TROPOMI sensors was presented. Here we concentrate on a global study of three years of HCHO observations

116 with TROPOMI, and we analyse their consistency with OMI data. Throughout the paper, we discuss the improved
117 capabilities of TROPOMI for the detection of HCHO at different temporal and spatial scales, from background
118 conditions to high emissions. We start with a few illustrations of the TROPOMI capabilities for HCHO monitoring
119 from space (sect. 3). We then provide a detailed comparison with the OMI QA4ECV HCHO dataset (sect. 4). In sect.
120 5, a global network of MAX-DOAS instruments is used to validate the OMI and TROPOMI HCHO datasets. Finally,
121 in sect. 6, we illustrate the enhanced capability of TROPOMI for the detection of very small HCHO emissions with
122 the identification of a signal over shipping lanes in the Indian Ocean.

123 2 HCHO Datasets

124 2.1 OMI instrument and QA4ECV HCHO product

125 The Aura satellite was launched in July 2004, in a low-Earth polar orbit crossing the equator at 13:30 LT. On board
126 ~~of~~ Aura, the Ozone Monitoring Instrument (OMI) is a nadir viewing imaging spectrometer that measures the solar
127 radiation backscattered by the Earth's atmosphere and surface over the wavelength range from 270 to 500 nm (Levelt
128 et al., 2006). Operational Level 2 (L2) products include vertical columns of O₃, SO₂, NO₂, HCHO, BrO, OCIO, as
129 well as cloud and aerosol information. OMI has a 2600 km wide swath (divided into 60 across-track positions or
130 rows), providing near-daily global coverage. However, due to a detector row anomaly that occurred after a few years
131 of operation, an increasing number of rows had to be filtered out leading to gradual degradation of the coverage. The
132 OMI ground pixel size varies from 13x24 km² at nadir to 28x150 km² at the edges of the swath.

133 The OMI QA4ECV HCHO product was developed by a European consortium (BIRA, IUP, MPIC, KNMI, WUR) (De
134 Smedt et al., 2017, <http://doi.org/10.18758/71021031>) in the framework of the EU-FP7 QA4ECV project. A detailed
135 step-by-step study was performed for HCHO and NO₂ retrievals as part of a community effort to homogenize GOME,
136 SCIAMACHY, GOME-2 and OMI, leading to state-of-the art European products (www.qa4ecv.eu). For this study,
137 we use the version 1.2 of the OMI HCHO dataset that is now spanning 15 years (2005-2020; Boersma et al., 2018;
138 Lorente et al., 2017; Nightingale et al., 2018; Zara et al., 2018). Note that within QA4ECV, a homogenized dataset of
139 NO₂ and HCHO MAX-DOAS reference measurements ([QA4ECV_MAXDOAS](#)) was also developed for satellite
140 validation (see sect. 2.4 and sect. 5).

141 2.2 TROPOMI instrument and the HCHO operational product

142 On board ~~of~~ the S5P platform, which - like Aura - flies in a low-Earth afternoon polar orbit with a local overpass time
143 of 13:30, the TROPOMI instrument is based on an imaging spectrometer measuring in the ultraviolet (UV), visible
144 (VIS), near-infrared (NIR), and shortwave infrared (SWIR) spectral regions (Veeffkind et al., 2012). Operational L2
145 products include vertical columns of O₃, SO₂, NO₂, HCHO, CO and CH₄, as well as cloud and aerosol information.
146 TROPOMI has a 2600 km wide swath (divided into 450 across-track positions or rows), providing near-daily global
147 coverage. The spatial resolution at nadir, originally of 3.5x7 km² (across-track x along-track) has been refined to
148 3.5x5.5 km² on 6 August 2019, by a change in the along-track integration time. The size of the pixels remains more
149 or less constant towards the edges of the swath (the largest pixels are ~14 km wide) ([L1b ATBD](#), [L1b readme file](#)).

150 The retrieval algorithm of the TROPOMI HCHO L2 product is directly inherited from the QA4ECV OMI algorithm
151 with the aim to create a consistent time series of early afternoon observations. For this study, we use a modified version
152 of the TROPOMI level-2 HCHO operational data product, which starts in April 2018 (phase E2, RPRO+OFFL,
153 product versions 1.1.[5-8]+2.1.3, doi: 10.5270/S5P-tjlxfd2). Product versions are described in the [Product Readme](#)
154 [File](#).

155 2.3 HCHO Retrieval algorithm for OMI and TROPOMI

156 The HCHO retrieval algorithm was fully described in De Smedt et al. (2018), and the successive adaptations of the
157 algorithm are reported in the S5P product ATBD. Here we only provide a short description of the algorithm, which is
158 based on a 3-steps DOAS method. First, the fit of the slant columns (N_s) is performed in the UV part of the spectra,
159 in the fitting interval 328.5-359 nm. The HCHO cross-section is from Meller and Moortgat (2000). All cross-sections
160 have been pre-convolved for every row separately with an instrumental slit function adjusted after TROPOMI launch.
161 For the OMI product, the slit function of each row is adjusted daily and the cross-sections are reconvolved accordingly.
162 The DOAS reference spectrum is updated daily with an average of Earth radiances measured in the Equatorial Pacific
163 region from the previous day. The fit therefore results in a differential slant column, corresponding to the HCHO
164 excess over sources compared to the remote background. In a second step, the conversion from slant to tropospheric
165 vertical columns (N_v) is performed using a look up table of vertically resolved air mass factors (M) calculated at 340
166 nm with the radiative transfer model VLIDORT v2.6 (Spurr, 2008). Entries for each ground pixel are the observation
167 geometry, the surface elevation and reflectivity, as well as clouds treated as reflecting surfaces, and a priori
168 tropospheric HCHO profiles. The surface albedo is taken from the monthly OMI albedo climatology at the spatial
169 resolution of $1^\circ \times 1^\circ$ (minimum LER, Kleipool et al., 2008). A priori vertical profiles are provided by the TM5-MP
170 daily analysis, at the spatial resolution of $1^\circ \times 1^\circ$ (Williams et al., 2017). A cloud correction based on the independent
171 pixel approximation (Boersma et al., 2004) is applied for cloud fractions (CF) larger than 0.1. Finally, to correct for
172 any remaining global offset and possible stripes arising between the rows, a background correction is performed based
173 on the HCHO slant columns in the Pacific Ocean ($N_{s,0}$). For the TROPOMI operational product, $N_{s,0}$ is based on the
174 four previous days. For this study, and for the OMI product, we perform the correction on the current day in order to
175 further reduce the stripes. To compensate for a background HCHO level in the Equatorial Pacific (due to the methane
176 oxidation), a vertical column of HCHO ($N_{v,0}^{CTM}$) is taken from the TM5 model in the reference region. The resulting
177 tropospheric HCHO vertical column can be written as follows:

$$N_v = \frac{N_s - N_{s,0}}{M} + \frac{M_0}{M} N_{v,0}^{CTM}, \quad (2-1)$$

178 with M_0 the air mass factor in the reference sector. Intermediate quantities and auxiliary data are all stored in the L2
179 files (see the product user manual for TROPOMI and OMI). Several diagnostic variables are provided together with
180 the measurements. The column averaging kernels and the a priori profiles are given for each observation. The
181 tropospheric column uncertainty is resolved into its random (precision) and systematic components (accuracy), and is
182 provided for every individual pixel.

183 The main difference between the OMI and TROPOMI algorithms lies in the cloud product that is used to compute air
184 mass factors. While the QA4ECV OMI product is based on the O₂–O₂ absorption feature around 477 nm, and considers
185 a fixed cloud albedo of 0.8 (version 2.0, Veeffkind et al., 2016), the TROPOMI product uses the S5P operational cloud
186 product in CRB (Cloud as Reflecting Boundary) mode (OCRA/ROCINN-CRB; Loyola et al., 2018). The S5P
187 ROCINN algorithm is based on the O₂ A-band around 760 nm and simultaneously retrieves cloud height and cloud
188 albedo. Systematic differences between the cloud parameters will result in differences in the air mass factors,
189 influencing the comparisons. To mitigate the impact of this difference between OMI and TROPOMI, we also switch
190 off the cloud correction by replacing the cloud-corrected AMF by an equivalent clear-sky AMF (M_{clear} , no cloud
191 correction applied) also provided in the L2 product. Based on equation (2-1(2-1)), the following simple transformation
192 can be applied:

$$N_{v_clear} = \frac{M}{M_{clear}} N_v \quad (2-2)$$

193 Note that this transformation has an effect on observations with cloud fractions comprised between 0.1 and 0.4. Indeed,
194 no cloud correction is applied for CF<0.1 and observations with CF>0.4 are filtered out from the analysis.

195 2.4 MAX-DOAS datasets

196 Multi-axis DOAS (MAX-DOAS) instruments retrieve the abundance of atmospheric trace species in the lowermost
197 troposphere (Hönninger et al., 2004; Wagner et al., 2004; Wittrock et al., 2004; Heckel et al., 2005). Based on DOAS
198 analyses (Platt and Stutz, 2008) of the scattered sky light under different viewing elevations, high sensitivity close to
199 the surface is obtained for the smallest elevation angles, whereas measurements at higher elevations provide
200 information on the rest of the column. MAX-DOAS measurements have been used in several studies to validate
201 satellite HCHO columns (Vigouroux et al., 2009; Franco et al., 2015; De Smedt et al., 2015; Chan et al, 2019; 2020;
202 Ryan et al., 2020; Kumar et al. 2020). However, a global network of MAX-DOAS instruments has not been used yet
203 for the validation of HCHO columns from space.

204 Ground-based data used in this study are presented in [Table 1](#). Apart from the QA4ECV MAX-DOAS dataset,
205 which relies on harmonized HCHO retrievals (Pinardi et al., 2013; QA4ECV [D3.8](#) and [D3.9](#),
206 <http://www.qa4ecv.eu/sites/default/files>), the MAX-DOAS data sets used here were generated by instrument principal
207 investigators using non-harmonised settings. The conversion to vertical columns and/or vertical profiles relies on
208 methods of various complexity levels. [Table 1](#) includes details about the retrieval strategy adopted by the
209 different teams. These include:

- 210 • GA: Geometrical approximation, the vertical column is determined using a single-scattering approximation
211 adequate for moderately high elevation angles α (typically 30°) so that a simple geometrical air-mass factor
212 ($AMF=SCD/VCD=1/\sin(\alpha)$) (Hönninger et al., 2004; Brinkma et al., 2008; Ma et al., 2013) can be used,
- 213 • QA4ECV: the vertical column is calculated using tropospheric AMFs based on climatological profiles and
214 aerosol loads as developed during the QA4ECV project ([QA4ECV_MAXDOAS_readmefile](#)). These data are
215 less sensitive to relative azimuth angle than the purely geometric approximation presented above,

Formatted: Font: 10 pt, Not Bold

Formatted: Font: 10 pt, Not Bold, Not Italic, Check spelling and grammar

Formatted: Font: 10 pt, Not Bold

Formatted: Font: 10 pt, Not Bold, Not Italic, Check spelling and grammar

- 216 • OEM: Vertical profile algorithms using an Optimal Estimation Method (Rodgers, 2000): these make use of a-
 217 priori vertical profiles and associated uncertainties (Friess et al., 2006; Clémer et al 2010; Hendrick et al., 2014;
 218 Gielen et al., 2017; Wang et al., 2019a; Friedrich et al., 2019; Bösch et al., 2018),
- 219 • PP: Vertical profile algorithms based on parameterized profile shape functions: these make use of analytical
 220 expressions to represent the trace gas profile using a limited number of parameters (Irie et al., 2009; 2011; Li et
 221 al., 2010; Vlemmix et al., 2010; Wagner et al., 2011; Beirle et al., 2019).

222 Both OEM and parameterized profiling approaches provide vertical profiles of aerosols and HCHO with good
 223 sensitivity in the 0-4 km altitude range, in which 1 to 3 independent pieces of information in the vertical dimension
 224 are available (Vlemmix et al., 2015; Friess et al., 2016; 2019). Recent intercomparison studies (Vlemmix et al., 2015;
 225 Friess et al., 2019; Tirpitz et al., 2021) show that both OEM and parameterized inversion approaches lead to consistent
 226 results in terms of tropospheric vertical columns but to larger differences in terms of profiles. The accuracy of the
 227 MAX-DOAS technique depends on the SCD retrieval noise, the uncertainty of the HCHO absorption cross-sections,
 228 the choice of the a-priori profile shape and the uncertainty of the tropospheric AMF calculation. MAX-DOAS HCHO
 229 slant columns from several instruments have been compared during international large-scale campaigns (CINDI-1 and
 230 2, e.g. Pinardi et al., 2013; Kreher et al., 2020) showing relatively large median differences and larger noise compared
 231 to other slant column products comparisons (e.g. NO₂). For HCHO, the slant column precision depends strongly on
 232 the signal-to-noise performance of the DOAS instrument with significantly better results for low-noise research-grade
 233 MAX-DOAS instruments (Pinardi et al., 2013; Kreher et al., 2020). The estimated total uncertainty on HCHO VCD
 234 is of the order of 30% to 60% in polluted conditions. This includes both random (~5% to 30% depending on
 235 instrumental signal-to-noise ratio) and systematic (20%) slant column contributions (Pinardi et al., 2013).

236 **Table 1: MAX-DOAS HCHO datasets included in the validation exercise. GA stands for geometrical approximation, OEM**
 237 **for Optimal Estimation Method and PP for Parametrized Profiling.**

Station, Country (lat/long)	Owner/ Group	Instrument Type	Retrieval Type	Reference
De Bilt, The Netherlands (52.10°N, 5.18°E)	KNMI	miniDOAS / Airyx	SCD and VCD from QA4ECV	Vlemmix et al., 2010 QA4ECV
Cabauw, The Netherlands (51.97°N, 4.93°E)	KNMI	miniDOAS/ Hoffmann	SCD and VCD from QA4ECV	QA4ECV
Uccle, Belgium (50.78° N, 4.35° E)	BIRA-IASB	Custom-built MAX-DOAS	VCD and profiles from OEM	Dimitropoulou et al, 2020
Xianghe, China (39.75° N, 116.96° E)	BIRA-IASB	Custom-built MAX-DOAS	VCD and profiles from OEM	Hendrick et al., 2014; Vlemmix et al., 2015
Mainz, Germany (50°N, 8.2°E)	MPIC	Custom-built MAX-DOAS	SCD and VCD from QA4ECV	Wang et al., 2017 QA4ECV
Munich, Germany (48,13_N, 11.58°E)	LMU	Airyx 2D MAX-DOAS	VCD and profiles from OEM	Chan et al. 2020
Mohali, India (30.67°N, 76.74°E)	IISER/MPIC	Custom-built MAX-DOAS	SCD and VCD from QA4ECV	Kumar et al., 2020 QA4ECV
Thessaloniki, Greece (40.63°N, 22.96°E)	AUTH	Phaethon	SCD and VCD from QA4ECV	Drosoglou et al., 2017 QA4ECV

Madrid, Spain (40.3°N, 3.7°W)	CSIC	MAX-DOAS	VCD and profiles from OEM	Benavent, et al., 2019.
Fukue, Japan (36.8°N, 128.7°E)	ChibaU	CHIBA-U MAX-DOAS	VCD and profiles from PP	Irie et al., 2011; 2012; 2015; 2019.
Chiba, Japan (35.63°N, 140.10°E)	ChibaU	CHIBA-U MAX-DOAS	VCD and profiles from PP	Irie et al., 2011; 2012; 2015; 2019.
Kasuga, Japan (33.52°N, 130.48°E)	ChibaU	CHIBA-U MAX-DOAS	VCD and profiles from PP	Irie et al., 2011; 2012; 2015; 2019.
Pantnagar, India (29°N, 79.47°E)	ChibaU	CHIBA-U MAX-DOAS	VCD and profiles from PP	Irie et al., 2011; 2012; 2015; 2019.
Phimai, Thailand (15.18°N, 102.56°E)	ChibaU	CHIBA-U MAX-DOAS	VCD and profiles from PP	Irie et al., 2011; 2012; 2015; 2019.
Xianghe, China (39.75° N, 116.96° E)	USTC	MAX-DOAS	VCD from OEM	
Beijing CAMS, China, (39.95°N, 116.32°E)	USTC	MAX-DOAS	VCD from GA	
UNAM, Mexico (19.33°N, 99.18°W)	UNAM	MAX-DOAS	VCD and profiles from OEM Eastwards pointing	Rivera Cardenas et al., 2021 Arellano et al., 2016
BroadMeadows, Australia (-37.7°, 144.9°)	Melbourne University ABM	Airyx	VCD from OEM	Ryan et al. 2018; 2020.

238 2.5 Data Use and Method

239 For this study, unless specified otherwise, we filter the satellite data based on the quality assurance values (QA)
240 ([Product Readme File](#)). QA>0.5 filters out most observations presenting an error flag or a solar zenith angle larger
241 than 70°, a cloud radiance fraction (CRF) at 340 nm larger than 0.6, an air mass factor smaller than 0.1, surface
242 reflectivity larger than 0.2, or an activated snow/ice flag. It should be noted that, in the first versions of the operational
243 product, the QA values were not correctly assigned over snow/ice regions, above 75° of SZA, and sometimes over
244 cloudy scenes. This issue has been corrected from version 2.1.3 (July 2020). For this study, we therefore reassigned
245 QA values using the above-mentioned filters.

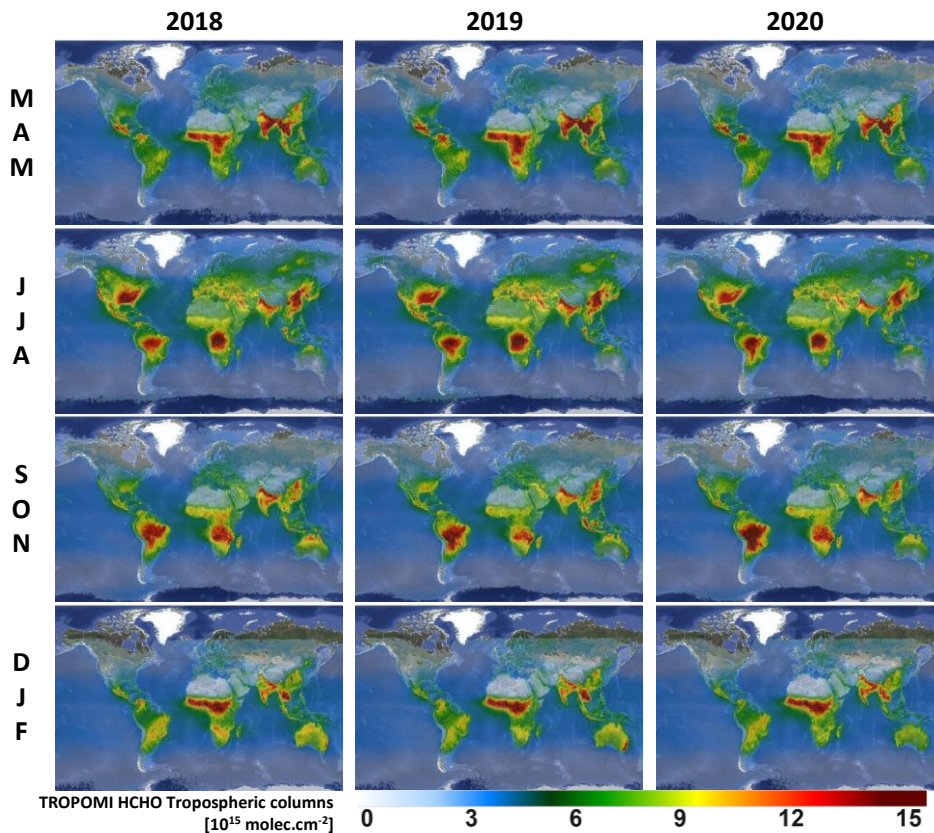
246 We calculated daily gridded data at a resolution of 0.05°x0.05° in latitude/longitude, both for OMI and TROPOMI,
247 using the [Harp atmospheric toolbox](#). ~~Along~~ Throughout the paper, daily and monthly averages are obtained from daily
248 grids. For each day, we require the region to be filled with a least 50% of valid grid cells, with a minimum of 10
249 TROPOMI observations (2 OMI observations).

250 For the satellite/satellite and the satellite/ground-based comparisons, we calculate the median of the absolute
251 differences (absolute bias) and the median of the relative differences (relative bias) in each region or station (relative
252 either to TROPOMI in the case of sat./sat. or to the MAX-DOAS columns in the case of sat./ground-based). The
253 corresponding median absolute-value deviations (MAD) of the absolute and relative differences are a robust estimate
254 of the combined observation and comparison variability. The MAD is defined as the median of the absolute-value
255 deviations from the data's median:

$$MAD = k \cdot \text{median}(\text{abs}(\text{Diff}_i - \text{median}(\text{Diff}_i))) \quad (2-3)$$

256 where the factor $k=1.4826$ is used to ensure a correspondence with the 1-sigma standard deviation for normal
 257 distribution. The bias is considered as statistically significant if it exceeds $ErrB=2*MAD/\sqrt{N}$, where N is the
 258 number of collocated pairs (days or months). We also derive correlation, slope and offset of the linear regression using
 259 the robust Teil-Shein estimator (Sen, 1968) as done in Vigouroux et al. (2020).

260 3 TROPOMI HCHO tropospheric columns



261 Figure 1: Seasonal maps of TROPOMI HCHO tropospheric columns during the three first years of measurements (March
 262 2018 – February 2021), on a spatial grid of 0.05° in latitude and longitude. Observations are filtered using the $qa_values > 0.5$.
 263 (max.scale: 15×10^{15} molec. cm^{-2}). Modified Copernicus Sentinel-5P satellite data, OFFL L2 HCHO product, BIRA-
 264 IASB/DLR/ESA/EU.

265 As an illustration of the data product, [Figure 1](#) displays the global seasonal distribution of tropospheric HCHO
 266 columns derived from TROPOMI observations between March 2018 and February 2021. The overall seasonality of
 267 the HCHO columns is largely driven by the emissions of NMVOCs from the vegetation and by the interannual
 268 variability of surface temperatures and solar radiation. As can be seen, in South Eastern US for example, the seasonal

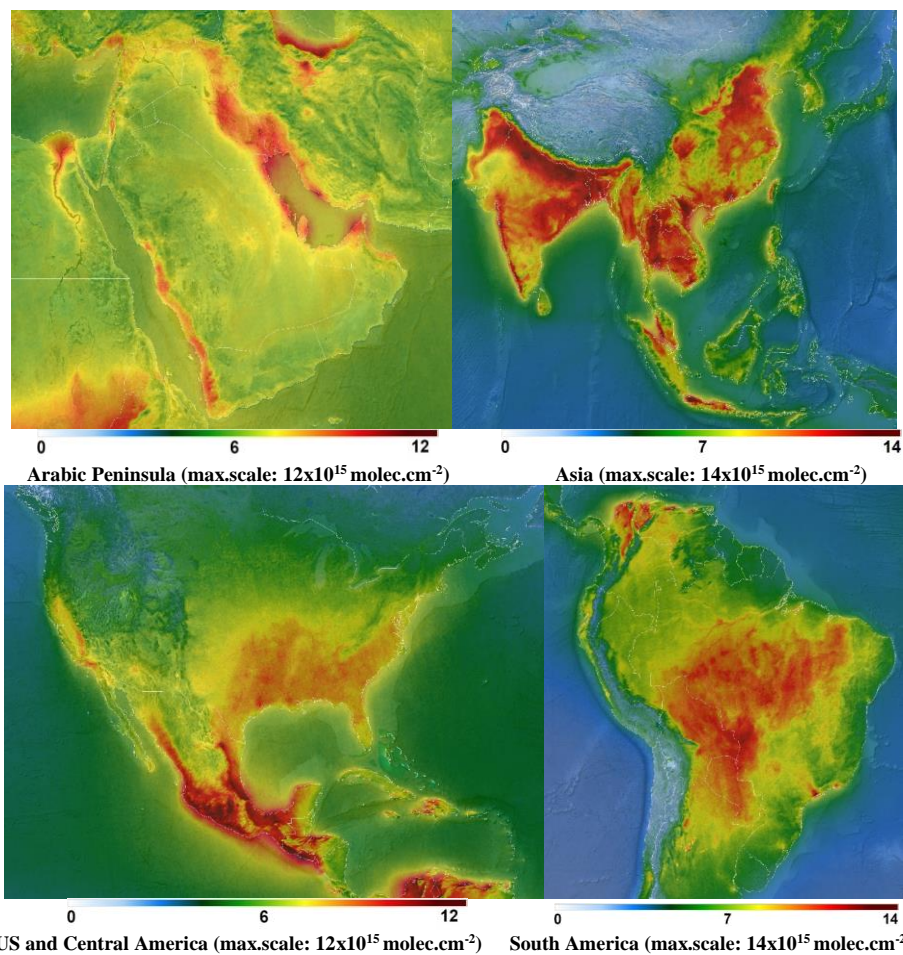
Formatted: Font: 10 pt, Not Bold
 Formatted: Font: 10 pt, Not Bold, Not Italic, Check spelling and grammar

269 amplitude is very important and dominated by biogenic emissions during summertime. On top of biogenic emissions,
270 wildfires present a large variability. Since 2018, many fire events occurred worldwide and can be traced e.g. in HCHO
271 columns during summer 2018 and 2020 in Western US, or during summer 2019 in Siberia. After a decrease of about
272 10 years (De Smedt et al., 2015), South America experienced two intense fire seasons in 2019 and 2020. The year
273 2020 was also marked by the huge Australian and Californian wildfires, respectively, in January and October 2020,
274 detectable in the seasonal maps. In comparison to biogenic and pyrogenic emissions of natural origin, the contribution
275 due to anthropogenic NMVOC emissions to the total HCHO columns is generally lower. Although their oxidation is
276 also enhanced by sunlight, anthropogenic emissions show less seasonality than natural emissions, and their detection
277 is therefore generally easier in annual maps. This is illustrated in ~~Figure 2~~ Figure 2, which presents 3-years averages
278 of HCHO columns over Asia, the Arabic Peninsula, the US and Central and South America, providing detailed
279 information about the spatial distribution of HCHO at the regional and urban scale. Europe and Africa are shown in
280 the supplement (fig.S1). Note that the colour scale has been adapted to the regions. Large urban areas are clearly
281 visible in the HCHO distribution in Asia, the Middle East and South America. With a lower magnitude, US cities are
282 also clearly detectable, such as Houston, Dallas or Los Angeles. HCHO levels are noticeably lower in Europe, but
283 some urban areas are visible in the Southern countries.

284 The quality of the TROPOMI observations also allows observing HCHO columns on a much shorter time scale with
285 an unprecedented definition. Daily observations of fire plumes are a clear step forward in the satellite remote sensing
286 of HCHO. They can be observed over much longer distances than before, thanks to the daily global coverage, coupled
287 with the finer spatial resolution and the improved signal to noise ratio, allowing ~~to detect~~ the detection of lower columns
288 transported further away (Alvarado et al. 2020; Theys et al. 2020). Not only wildfires, but also important
289 anthropogenic emission plumes can be observed on a daily basis, for example on the Eastern coast of Saudi Arabia.
290 A few illustrations are given in fig.S2. The TROPOMI performances for the observations of HCHO are discussed
291 more quantitatively along the paper in terms of precision and bias, as a function of the HCHO levels, and of the
292 temporal and spatial scales.

Formatted: Font: 10 pt, Not Bold

Formatted: Font: 10 pt, Not Bold, Not Italic, Check spelling and grammar



294 Figure 2: Multi-annual regional maps of TROPOMI HCHO tropospheric columns (March 2018 – February 2021), on a
 295 spatial grid of 0.05° in latitude and longitude. Observations are filtered using the $qa_values > 0.5$. Modified Copernicus
 296 Sentinel-5P satellite data, OFFL L2 HCHO product, BIRA-IASB/DLR/ESA/EU.

297 4 Comparison between OMI and TROPOMI measurements

298 In this section, we evaluate the consistency between OMI and TROPOMI HCHO tropospheric columns. In addition,
 299 we present the gain in precision obtained with TROPOMI. The analysis relies on 32 months of simultaneous
 300 measurements from April 2018 to December 2020, allowing for a meaningful comparison at different scales. We first

301 compare the precision obtained on individual measurements, and then proceed with a comparison of the precisions
302 achieved when averaging data at different spatial and temporal scales.

303 4.1 HCHO slant column precision

304 The random uncertainty of the tropospheric HCHO column is dominated by the error on the fitted slant column
305 densities (SCDE) which is directly related to the signal to noise ratio (SNR) of the measurement. From this point of
306 view, TROPOMI performs significantly better than previously launched nadir UV-VIS satellite instruments. In the
307 spectral range of HCHO retrievals (328.5-359 nm), the SNR of the TROPOMI spectra exceeds pre-flight requirements
308 that were based on OMI specifications (Kleipool et al., 2018; Ludewig et al., 2020).

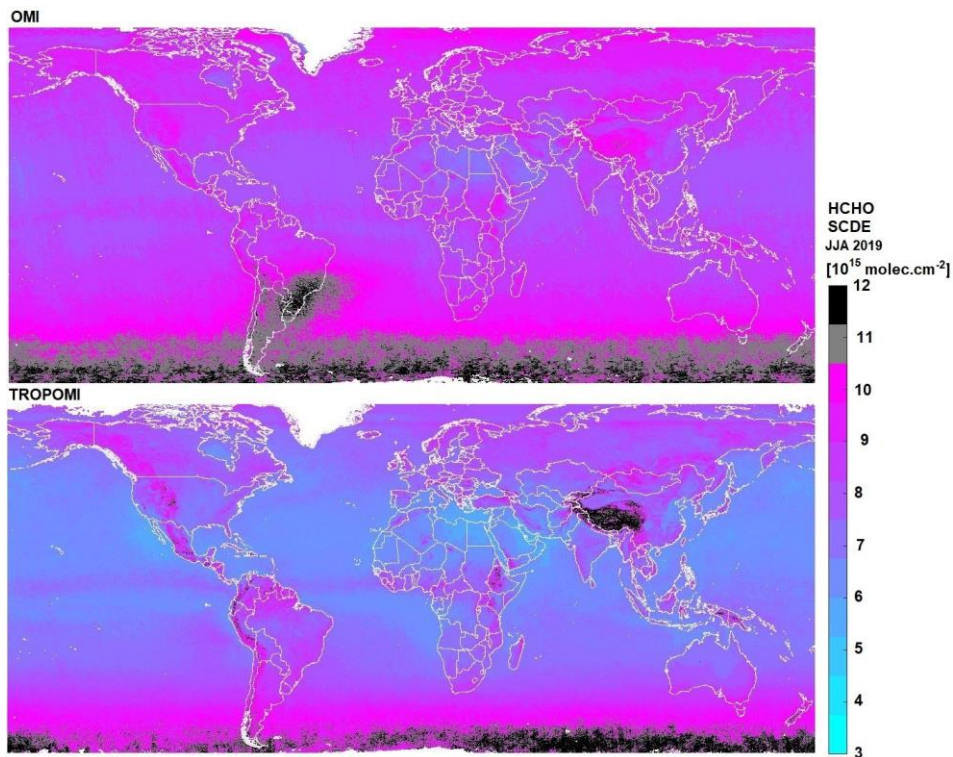
309 ~~Figure 3~~ **Figure 3** presents global maps of SCDE averaged over 3 months during summer 2019, from OMI and
310 TROPOMI. From the improved SNR of TROPOMI in the UV range, TROPOMI HCHO SCDEs of individual
311 observations are about 25% lower than OMI ones. Over remote areas, the TROPOMI SCDE is about 6×10^{15} molec.cm⁻²,
312 while it is 8×10^{15} molec.cm⁻² for OMI. Slant column density errors are also improved over emission areas and at
313 larger SZA. Contrary to OMI, the effect of the South Atlantic Anomaly is absent in TROPOMI SCDE. This probably
314 results from a better shielding of the instrument against extra-terrestrial high energy radiation. The implemented
315 iterative spike algorithm (De Smedt et al., 2018) is also more efficient because of the lower noise level of the
316 instrument. Note however that over mountains, TROPOMI SCDE are higher than OMI ones. The most obvious effect
317 is observed over the Himalayans, but other chains such as the Andes or the Rocky mountains are also affected. This
318 effect has been identified as a scene inhomogeneity effect (Richter et al., 2018; 2020). The effect is also visible along
319 the borders of bright lakes or white surfaces. OMI retrievals are also affected by scene inhomogeneity effects, but the
320 larger size of the ground pixels and the larger mean SCDE values make its detection more difficult. We note that in
321 the ~~long-term~~ **3-year** averaged maps of the HCHO tropospheric columns, some collocated artefacts appear (**Figure**
322 ~~2~~ **Figure 2**, e.g. the white sands in the US, Tuz Golu lake in Turkey or Lake Mackay in Australia). Most of the snow/ice
323 scenes are eliminated by the quality assurance values. The observations could however be better filtered over
324 mountains and along the lake borders, or even corrected during the fit of the slant columns as demonstrated for NO₂
325 and glyoxal (Lerot et al., 2021, in prep.). The relatively coarse albedo climatology also needs to be updated with a
326 TROPOMI-based product, better defined in space and time (Loyola et al., 2020).

Formatted: Font: 10 pt, Not Bold

Formatted: Font: 10 pt, Not Bold, Not Italic, Check spelling and grammar

Formatted: Font: 10 pt, Not Bold

Formatted: Font: 10 pt, Not Bold, Not Italic, Check spelling and grammar

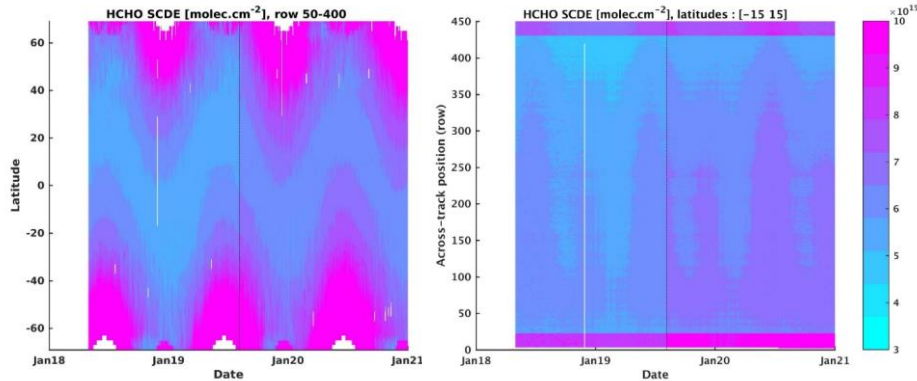


327
 328 **Figure 3: Average HCHO slant column density fitting error (SCDE) retrieved from OMI (upper panel) and TROPOMI**
 329 **(lower panel) in JJA 2019, on a spatial grid of 0.05° in latitude and longitude.**

330 The OMI SCDEs have been very stable over the years, showing a limited increase of about 5% between 2005 and
 331 2019 (De Smedt et al., 2018). However, the number of valid OMI observations has decreased by about 30% during
 332 the same period (-50% at large SZA) due to the row anomaly. In order to evaluate the stability of the TROPOMI
 333 HCHO retrievals during the three first years, [Figure 4](#) presents the time series of the TROPOMI HCHO slant
 334 column errors in the remote Pacific Ocean as a function of latitude and instrumental rows. As expected, we observe
 335 an increase of the noise for large SZAs, and for the 25 first and last rows of the scan, which have a different detector
 336 binning ([L1b ATBD](#)). The fact that the algorithm makes use of daily updated radiances as reference for the DOAS fit
 337 allows for very stable results in time and across the rows. Only the change in pixel size in August 2019 ([L1b readme](#)
 338 [file](#)) resulted in a moderate step increase of the SCDE of about 15%. These values are compared to the observed
 339 standard deviation of the slant columns in the same regions (see fig.S3). We observe a very good agreement between
 340 the SCDEs and the standard deviation, indicating that they give a good representation of the random errors.
 341 The reported uncertainty on the tropospheric vertical columns due to random errors corresponds to the SCDE divided
 342 by the AMF for each observation. In the Equatorial Pacific, the TROPOMI vertical column precision is about 5×10^{15}

Formatted: Font: 10 pt, Not Bold
Formatted: Font: 10 pt, Not Bold, Not Italic, Check spelling and grammar

343 molec.cm⁻², while it is 7x10¹⁵ molec.cm⁻² for OMI. It is larger over continental emissions, where the AMFs are
 344 generally smaller than 1.



345 **Figure 4:** TROPOMI HCHO slant column density errors (SCDE) as a function of the latitude (left column) or the detector
 346 row (right column). The step increase on 6th August 2019 reflects the change in the TROPOMI pixel size (indicated with
 347 the black line).

348 **4.2 HCHO tropospheric columns**

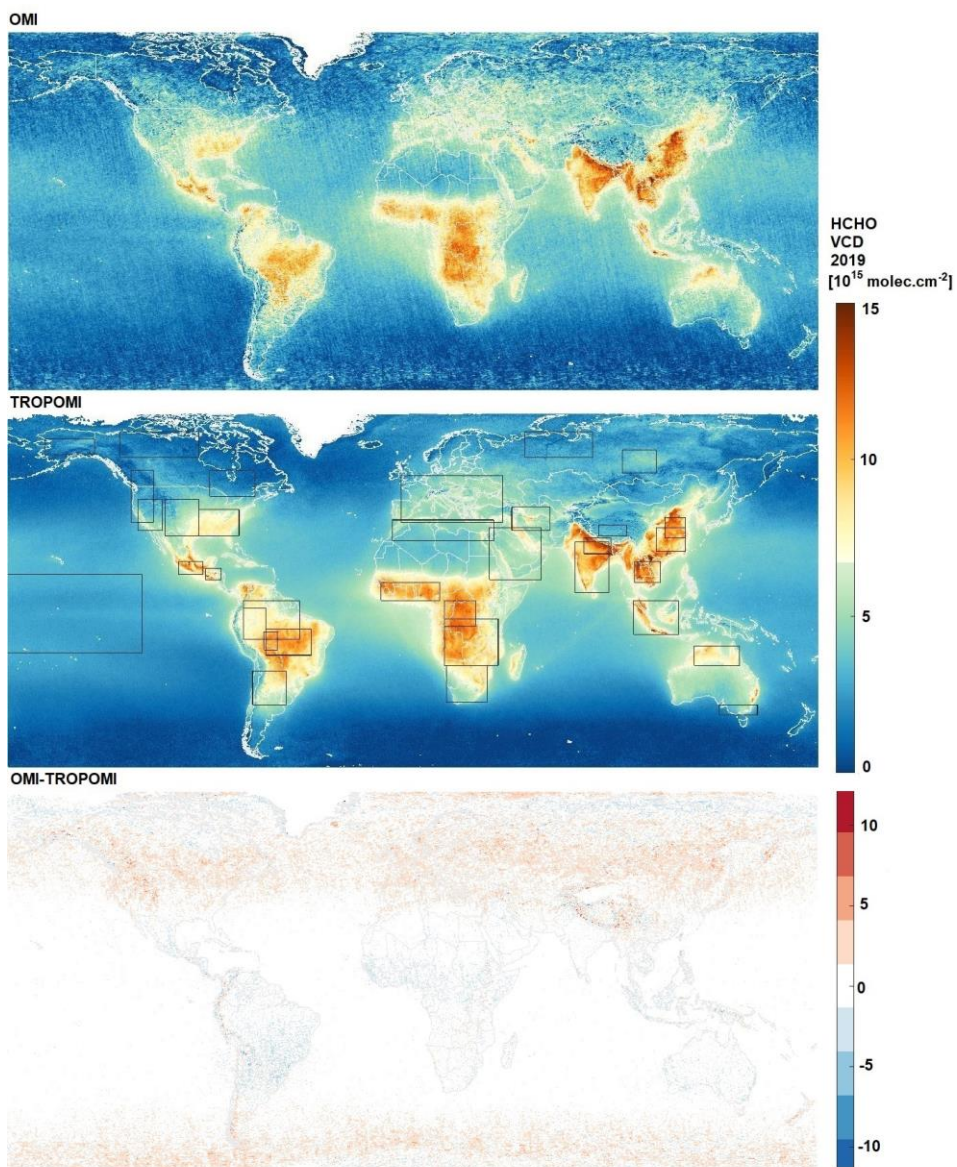
349 Figure 5 presents the yearly averaged OMI and TROPOMI HCHO vertical columns ($N_{v, clear}$) for 2019. Even
 350 at this level of averaging, the lower noise level of TROPOMI is very clear, especially for low to medium HCHO
 351 levels. We observe an overall good agreement of the columns both in magnitude and in their spatial distribution.
 352 Differences of TROPOMI and OMI yearly averages range from +2x10¹⁵ molec.cm⁻² over Tropics to -2x10¹⁵ molec.cm⁻²
 353 over mid-latitude regions. Differences tend to increase with latitudes. However, as the quality of the TROPOMI
 354 observations is improved at large solar zenith angles, more data in winter months are kept in the TROPOMI dataset,
 355 which can influence yearly averaged columns at those latitudes. In order to provide quantitative comparisons, we
 356 calculated daily and monthly averaged columns in 35 regions covering a broad range of emission levels and
 357 observation conditions (large black boxes on Figure 5). As the regions are large, many observations are
 358 included (on average 500/day for OMI, 12500/day for TROPOMI). To obtain daily and monthly comparison pairs,
 359 we keep coincident days of observations and follow the methodology presented in sect. 2.5.

Formatted: Font: 10 pt, Not Bold

Formatted: Font: 10 pt, Not Bold, Not Italic, Check spelling and grammar

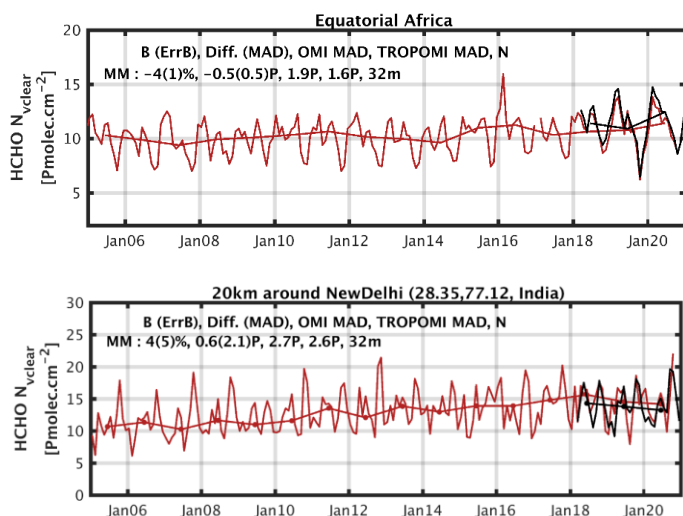
Formatted: Font: 10 pt, Not Bold

Formatted: Font: 10 pt, Not Bold, Not Italic, Check spelling and grammar



360
361 Figure 5: Average HCHO tropospheric column ($N_{v,clear}$) retrieved from OMI (first line) and TROPOMI (second line) in
362 2019. Limits of the regions selected for the comparisons are shown on the TROPOMI map. Differences between OMI and
363 TROPOMI maps are shown on the last panel. The same grid is used for both dataset (0.05°). Data are filtered using the
364 product quality flags. The large black boxes on the TROPOMI maps represent the regions used in the comparisons (see
365 [Figure 6](#) and [Figure 7](#)).

366 An example of a time series over Equatorial Africa is presented on the first panel of [Figure 6](#), where monthly
 367 averaged N_{v_clear} are shown, and comparison numbers are provided in the inset. In the Equatorial African region, the
 368 seasonal cycle is marked by two peaks during the dry seasons and two minima during the wet seasons. In 2019, the
 369 minimum was particularly low, observed in both the OMI and TROPOMI timeseries, while the maxima tend to
 370 increase over the years. More examples of time series can be found in fig.S4. In all the regions, the seasonal and
 371 interannual variability of the HCHO columns are observed very consistently with OMI and TROPOMI.



372 **Figure 6:** Examples of monthly and yearly averaged HCHO columns (N_{v_clear}) retrieved from OMI (Oct.2004-Dec.2020, in
 373 red) and TROPOMI (2018-Dec.2020, in black) at two different spatial scales selected for the comparison: a large region of
 374 Equatorial Africa, and a circle of 20km-radius over New Delhi in India. Absolute and relative biases between OMI and
 375 TROPOMI HCHO monthly averaged columns are given in inset, as well as the median deviations of the OMI and
 376 TROPOMI averaged columns. [$\text{Pmolec.cm}^{-2} = 1 \times 10^{15} \text{ molec.cm}^{-2}$].

377 [Figure 7](#) presents the absolute and relative biases between OMI and TROPOMI HCHO tropospheric columns
 378 for all regions. Numbers are provided for daily averaged columns applying a cloud correction (N_v) or not (N_{v_clear}).
 379 Regions are sorted as a function of the averaged TROPOMI HCHO column. At this large spatial scale, the regions
 380 over Equatorial Africa, Northern China and Northern India present the largest annual columns worldwide, with median
 381 levels larger than $10 \times 10^{15} \text{ molec.cm}^{-2}$. Tropical regions in South America, Africa and Asia present elevated levels of
 382 HCHO as well, with annual averaged columns larger than $8 \times 10^{15} \text{ molec.cm}^{-2}$.

383 Looking at N_v comparisons, it appears that the OMI HCHO columns present a positive bias compared to TROPOMI
 384 from $17 \pm 2.5\%$ for the columns larger than $5 \times 10^{15} \text{ molec.cm}^{-2}$, to $30 \pm 5\%$ for the lower columns. This bias exceeds
 385 50% in Northern latitudes ($>45^\circ$) and low-emissions ($<2 \times 10^{15} \text{ molec.cm}^{-2}$) regions of Canada and Alaska. However,
 386 when comparing N_{v_clear} , the biases are strongly reduced below 10% in all regions where the HCHO levels are larger
 387 than $5 \times 10^{15} \text{ molec.cm}^{-2}$, and the TROPOMI columns are found to be slightly larger than OMI on average ($-3 \pm 1.2\%$).
 388 In mid-Northern-latitudes/moderate emissions ($2-5 \times 10^{15} \text{ molec.cm}^{-2}$) regions such as Europe, Central and Western

Formatted: Font: 10 pt, Not Bold

Formatted: Font: 10 pt, Not Bold, Not Italic, Check spelling and grammar

Formatted: Font: 10 pt, Not Bold

Formatted: Font: 10 pt, Not Bold, Not Italic, Check spelling and grammar

389 US, North Western Canada, Siberia or Tibet, OMI columns present a remaining bias of about $15\pm 3\%$, while in the
390 regions of Canada and Alaska, a larger bias of about $+30\pm 7\%$ remains. Note that we observe biases lower than 10%
391 in the Maghreb and Southern Australia regions, despite their relatively low columns or low latitudes.

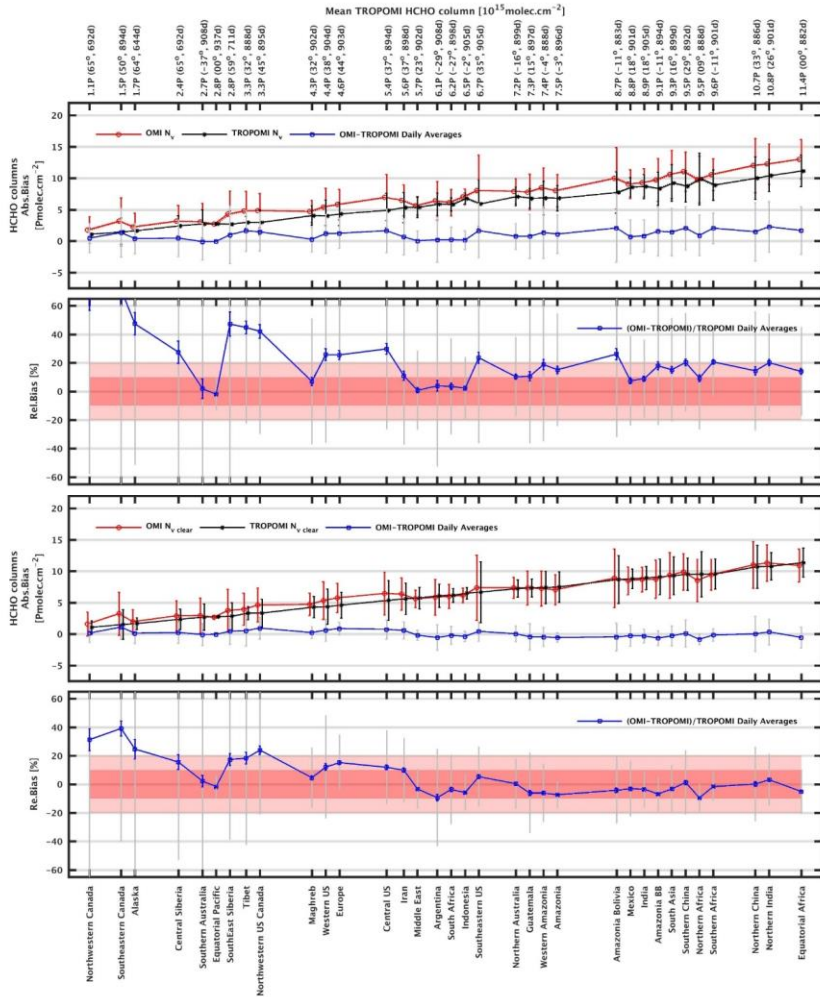
392 We conclude that biases up to 30% related to the cloud correction are observed over Tropical regions where the clouds
393 are the highest in altitude (Africa, South America, South Asia), and a smaller but systematic effect, up to 15%, is
394 observed over mid-latitude polluted regions such as China, India, US or Europe. We also note that the differences
395 between N_v and N_{v_clear} are mainly significant for the OMI HCHO columns. It has been reported that the cloud
396 pressures retrieved from TROPOMI and from OMI present a bias (OMI clouds are higher in altitude, Compernelle et
397 al., 2020). This translates into OMI cloud-corrected air mass factors generally smaller than TROPOMI AMFs by 5 to
398 30%, depending on the cloud altitude, and therefore in a positive bias of the OMI HCHO VCD compared to the
399 TROPOMI product. It is therefore important to keep in mind that the use of different cloud products may introduce
400 inconsistencies, which may be resolved by using clear HCHO VCDs (N_{v_clear}).

401 Figure 8 shows the linear regression between OMI and TROPOMI monthly averaged columns, considering
402 all regions together. The relation between OMI and TROPOMI is provided for N_v and N_{v_clear} . This shows that
403 switching off the cloud correction in the OMI and TROPOMI HCHO products allows to significantly improve not
404 only the slope (from 0.87 to 0.92) and the intercept (from 1.52 to 0.48×10^{15} molec.cm⁻²), but also the data scatter, i.e.
405 the Pearson R correlation (from 0.74 to 0.98). When considering large-scale comparisons, the agreement between
406 OMI and TROPOMI N_{v_clear} is therefore very satisfactory.

Formatted: Font: 10 pt, Not Bold

Formatted: Font: 10 pt, Not Bold, Not Italic, Check spelling and grammar

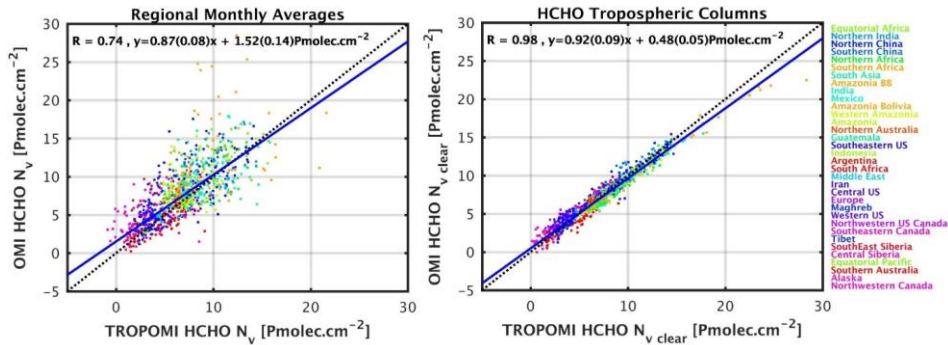
407



408

409 Figure 7: Absolute and relative biases between OMI and TROPOMI HCHO daily averaged tropospheric columns using
 410 cloud corrected AMF (N_v , two upper panels) or clear sky AMF ($N_{v,clear}$, two bottom panels) for the large regions
 411 represented on Figure 5. Regions are sorted as a function of the median TROPOMI HCHO column. Values of the
 412 averaged HCHO columns are provided on the top axis, as well as the numbers of common days taken for the comparison
 413 and the latitude of the region. The median OMI (red) and TROPOMI (black) columns are plotted together with the absolute
 414 differences (in blue). Error bars represent the median deviations of the columns, or the median absolute deviations of the

415 differences (MAD, in grey). Statistical ErrB are also plotted for the relative bias (in blue). Pink areas indicate 10% and
 416 20% bias. [$\text{Pmolec.cm}^{-2} = 1 \times 10^{15} \text{ molec.cm}^{-2}$].



417
 418 **Figure 8:** Scatter plots of OMI versus TROPOMI columns for the monthly means of collocated data. Results are shown for
 419 N_v (left panel) and $N_{v,clear}$ (right panel). The correlation, slope and intercept of a linear regression using the robust Teil-
 420 Shein estimator are given as inset and plotted as a blue line. Black dotted line is the 1:1 line. The color indicates the latitude
 421 of the region. [$\text{Pmolec.cm}^{-2} = 1 \times 10^{15} \text{ molec.cm}^{-2}$].

422 When averaging data over large regions, the dispersion due to random uncertainties is greatly reduced compared to
 423 individual observations. As summarized in [Table 2](#), the median absolute deviations of the monthly averaged
 424 columns are equivalent for OMI and TROPOMI ($1.8 \times 10^{15} \text{ molec.cm}^{-2}$), while the MAD of their differences are
 425 significantly lower ($0.5 \times 10^{15} \text{ molec.cm}^{-2}$). This indicates that at this spatiotemporal resolution, the natural variability
 426 dominates the dispersion of the averaged observations. Looking at the daily averaged columns, the TROPOMI median
 427 deviation is lower than for OMI (2.2/2.7), but still larger than the MAD of their differences (1.5).

428 The improved spatial resolution of TROPOMI should allow for a better detection of localized HCHO
 429 emissions columns. To address this question, we performed the same comparisons as for the large regions, but looking
 430 at smaller areas of 20km radius around cities. [Figure 9](#) presents the absolute and relative biases of the monthly
 431 averaged HCHO columns ($N_{v,clear}$) for a large number of cities. At this spatial scale, Jakarta is the location with the
 432 largest median HCHO level ($>18 \times 10^{15} \text{ molec.cm}^{-2}$ over the 2018-2020 period). Indian, Chinese and other Asian cities
 433 follow, as well as Mexico, Monterrey or Kinshasa ($>12 \times 10^{15} \text{ molec.cm}^{-2}$). Sao Paulo, Tehran and Cairo present also
 434 noticeably elevated HCHO levels ($>9 \times 10^{15} \text{ molec.cm}^{-2}$). An example over New Delhi is presented on the second panel
 435 of [Figure 6](#) and more examples can be found in [fig.S5](#).

436 When comparing OMI and TROPOMI $N_{v,clear}$ around the cities, the same general behaviour as in the large regions
 437 can be observed. OMI presents a positive bias ($20 \pm 15\%$) compared to TROPOMI for low to medium HCHO levels,
 438 while for medium to large levels, the agreement is very good on average ($-1 \pm 10\%$). There are nevertheless a few
 439 exceptions where TROPOMI HCHO columns are significantly larger than the OMI ones. This is the case at La
 440 Reunion, Paramaribo, Nairobi, Bujumbura, Sao Paulo, Monterrey, Mexico, or Jakarta. Those cities are located along
 441 marine coasts or lakes, at higher altitude, or are surrounded by mountains. In those cases, the finer spatial resolution
 442 of TROPOMI clearly improves the detection of the HCHO signal. For most other locations, however, the impact of
 443 the improved spatial resolution of TROPOMI on the HCHO columns is not detectable in the column magnitudes,

Formatted: Font: 10 pt, Not Bold

Formatted: Font: 10 pt, Not Bold, Not Italic, Check spelling and grammar

Formatted: Font: 10 pt, Not Bold

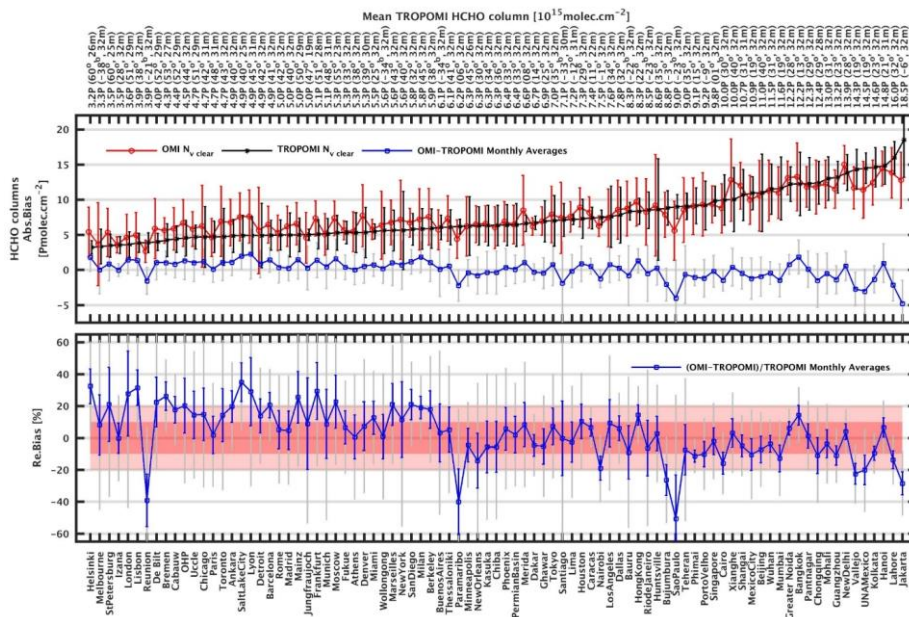
Formatted: Font: 10 pt, Not Bold, Not Italic, Check spelling and grammar

Formatted: Font: 10 pt, Not Bold

Formatted: Font: 10 pt, Not Bold, Not Italic, Check spelling and grammar

444 when compared to OMI observations. This is likely related to the nature of the HCHO production that mostly is
 445 secondary from the oxidation of NMVOCs with various lifetimes (Stavrakou et al. 2015; Bauwens et al., 2016). Except
 446 for regions where the topography presents sharp discontinuities, this causes a natural spread of the HCHO columns at
 447 a scale larger than the TROPOMI spatial resolution.
 448 Note however that at this spatial resolution (20km radius), the level of noise is larger than for the regional averages
 449 and the TROPOMI averaged columns are significantly more stable than the OMI ones, as evidenced by their median
 450 deviations (see [Table 2](#)). On a daily basis, the OMI columns present a dispersion of 7.8×10^{15} molec.cm⁻², while the
 451 TROPOMI dispersion is about twice smaller (3.7×10^{15} molec.cm⁻²). In this case, the MAD of the differences (7.1×10^{15}
 452 molec.cm⁻²) is dominated by the noise on OMI observations. Note that these estimates still include the natural
 453 variability of the columns themselves. If an area of 20-km radius in the remote Equatorial Pacific is considered, the
 454 observations represent constant background values and the seasonal variability is further reduced. In such conditions,
 455 the dispersion of the OMI daily observations is 3.5×10^{15} molec.cm⁻², while only 1×10^{15} molec.cm⁻² for TROPOMI.
 456 We show in the next section that validation with ground-based measurements brings further information on the satellite
 457 column precision.

Formatted: Font: 10 pt, Not Bold
 Formatted: Font: 10 pt, Not Bold, Not Italic



458
 459 **Figure 9: Absolute and relative biases between OMI and TROPOMI HCHO monthly averaged tropospheric columns using**
 460 **clear sky AMF ($N_{v,clear}$) within 20km-radius circles around selected cities, sorted as a function of the median TROPOMI**
 461 **HCHO column. Value of the averaged HCHO columns are provided on the top axis, as well as the numbers of months taken**
 462 **for the comparison, and the latitude of the region. The median OMI (red) and TROPOMI (black) columns are plotted**
 463 **together with the absolute differences (in blue). Error bars represent the median absolute deviations (MAD) of the columns**
 464 **and of the differences (in grey). Statistical ErrB are also plotted for the relative bias (in blue). Pink areas indicate 10% and**
 465 **20% bias. [Pmolec.cm⁻² = 1×10^{15} molec.cm⁻²].**

466 Table 2: Median absolute deviation of the OMI and TROPOMI daily and monthly averaged columns ($N_{v,clear}$), in large
 467 regions and in 20km-radius area. MAD of differences between OMI and TROPOMI columns are also given in the last
 468 column.

Dispersion	OMI MAD [10^{15} molec.cm ⁻²]	TROPOMI MAD [10^{15} molec.cm ⁻²]	OMI-TROPOMI MAD [10^{15} molec.cm ⁻²]
Monthly Regional	1.8	1.8	0.5
Daily Regional	2.7	2.2	1.6
Monthly 20km	3.3	2.5	2.4
Daily 20km	7.8	3.7	7.1
Daily 20km in the Equatorial Pacific	3.5	1.0	3.7

469 **5 Validation with a global MAX-DOAS network**

470 Here, we present a validation exercise based on a network of 18 ground-based MAX-DOAS instruments. This effort
 471 complements the study of Vigouroux et al. (2020), which relied on a network of FTIR instruments. Compared to the
 472 FTIR instruments, the MAX-DOAS provide a higher sensitivity in the boundary layer, where the bulk of HCHO is
 473 located. The MAX-DOAS network covers stations where the level of HCHO is significant, from medium to very large
 474 HCHO columns, while the FTIR network includes a larger number of remote stations. In this study, we validate in
 475 parallel the OMI and TROPOMI datasets. We first focus on a direct comparison of the satellite and MAX-DOAS
 476 tropospheric columns. The effect of the vertical smoothing is investigated in the next subsection for three stations.

477 **5.1 Direct comparisons of tropospheric columns**

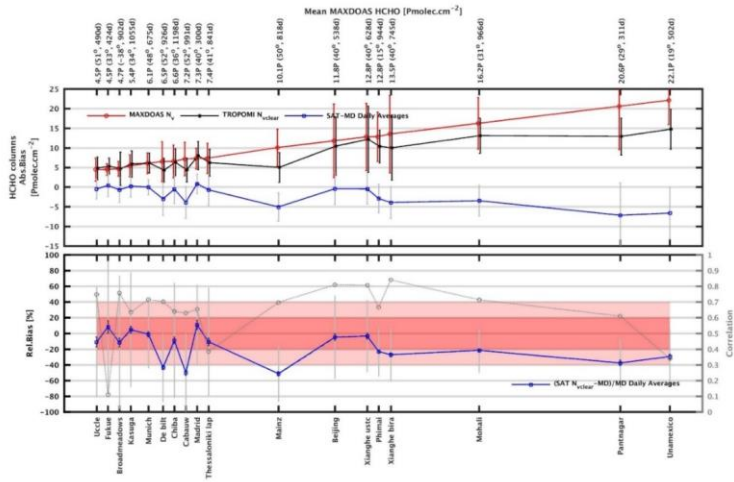
478 For each station in [Table 1](#), we consider daily averages of the satellite columns in a radius of 20km around the
 479 instruments. We average MAX-DOAS columns between 11h and 16h local time. We keep coincident days of
 480 observations (OMI/MAX-DOAS, TROPOMI/MAX-DOAS) to obtain daily and monthly comparison pairs. Note that
 481 the time periods used for the comparison are not the same for OMI and TROPOMI, and vary between the stations. To
 482 obtain the validation results, we follow the methodology presented in Vigouroux et al. (2020) (see sect. 2.5).

Formatted: Font: 10 pt, Not Bold

Formatted: Font: 10 pt, Not Bold, Not Italic, Check spelling and grammar

483

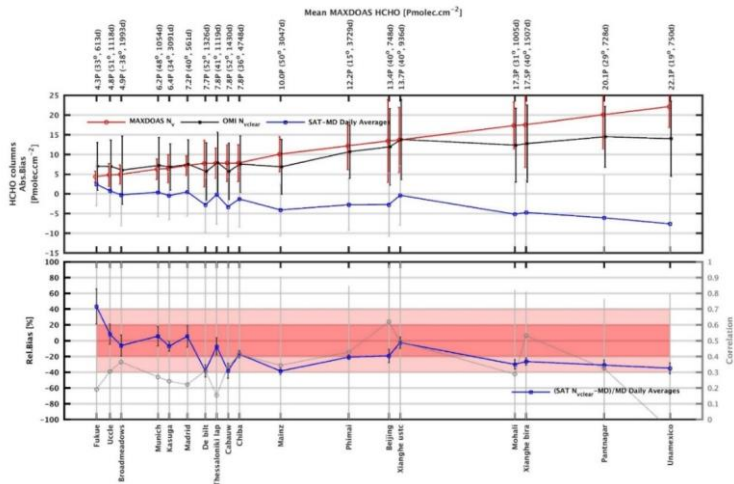
484 Figure 10: Absolute (top, blue line) and relative biases (bottom) between MAX-DOAS and TROPOMI HCHO daily
 485 averaged tropospheric columns in a circle of 20km-radius around the stations. Regions are sorted as a function of the
 486 median MAX-DOAS HCHO column. In the upper plot, the median MAX-DOAS (red) and TROPOMI (black) columns are
 487 plotted together with the differences. Error bars (in grey) represent the median absolute deviations (MAD) of the columns
 488 and of the differences. Statistical ErrB are also plotted for the relative bias (in blue). Pink areas indicate 20% and 40%
 489 bias. The correlation between the daily observations are given in the lower plot (grey circles). [$\text{Pmolec.cm}^{-2} = 1 \times 10^{15}$
 490 molec.cm^{-2}].



491

492 Figure 11: same as Figure 10 for MAX-DOAS and OMI HCHO daily averaged.

493



494 ~~Figure 10~~ Figure 10 and ~~Figure 11~~ Figure 11 present the absolute and relative biases of the daily averaged columns as
495 a function of the median MAX-DOAS HCHO column, respectively, for TROPOMI and OMI. A more detailed
496 description for each station and for individual time series is presented afterwards. The values of the biases are similar
497 for OMI and TROPOMI, except for the lowest columns in Uccle and Fukue, where OMI presents larger positive biases
498 exceeding +20%. In agreement with Vigouroux et al. (2020), TROPOMI columns do not present a significant bias for
499 the range of HCHO levels from 4 to 8×10^{15} molec.cm⁻². Note that, in contrast to FTIR data, the range of values covered
500 by our MAX-DOAS network does not extend to columns lower than 4×10^{15} molec.cm⁻². We observe that the stations
501 in De Bilt and Cabauw tend to show somewhat stronger negative biases even for medium levels of HCHO, which
502 might point to a network inhomogeneity. For larger HCHO columns ($> 8 \times 10^{15}$ molec.cm⁻²), and in agreement with the
503 FTIR results, we observe that negative biases tend to increase for large HCHO columns such that the underestimation
504 of the satellite columns reaches about -40% for the largest columns. On the upper plot, the error bars represent the
505 median absolute deviations of the columns and of their differences. It appears clearly that the MADs obtained with
506 TROPOMI are substantially lower than those obtained with OMI. Note that the type of MAX-DOAS instrument (in
507 particular its signal-to-noise ratio) may also influence the observed MAD at the different stations.

508 ~~Figure 12~~ Figure 12, ~~Figure 13~~ Figure 13 and ~~Figure 14~~ Figure 14 present more detailed results for the stations in
509 Europe, Japan and Australia, and China, India, Thailand and Mexico, respectively. On each plot, the time series of the
510 MAX-DOAS, OMI and TROPOMI data are displayed together. Results of the daily statistical analysis are given as
511 inset. At European stations, which show medium range HCHO levels, we obtain contrasted results. With a mean
512 HCHO column of 4.5×10^{15} molec.cm⁻², Uccle is one of the stations with the lowest columns of the network presented
513 in this paper. While OMI values show a positive bias ($13 \pm 15\%$) and a poor correlation (0.3) with the MAX-DOAS,
514 TROPOMI appears to be biased low ($-10 \pm 6\%$) but much better correlated (0.82) with the MAX-DOAS data. As
515 opposed to Uccle, the observed biases in De Bilt, Cabauw, and Mainz are largely negative (from -40% to -50%). The
516 correlations found with TROPOMI are nevertheless much better than with OMI. Note that the median MAX-DOAS
517 HCHO value in Mainz is larger than 10×10^{15} molec.cm⁻², which is quite high for an European site. The results in
518 Munich have been presented in details in Chan et al. (2020). They are closer to what is found in Uccle, with a small
519 positive bias for TROPOMI ($1 \pm 3\%$) and for OMI ($6 \pm 13\%$). Similarly in Madrid, OMI and TROPOMI results are very
520 consistent with a mean bias of respectively $8 \pm 16\%$ and $10 \pm 6\%$. In Thessaloniki, the negative bias is $-12 \pm 5\%$, but the
521 correlation is poorer than in Madrid.

Formatted: Font: 10 pt, Not Bold

Formatted: Font: 10 pt, Not Bold, Not Italic, Check spelling and grammar

Formatted: Font: 10 pt, Not Bold

Formatted: Font: 10 pt, Not Bold, Not Italic, Check spelling and grammar

Formatted: Font: 10 pt, Not Bold

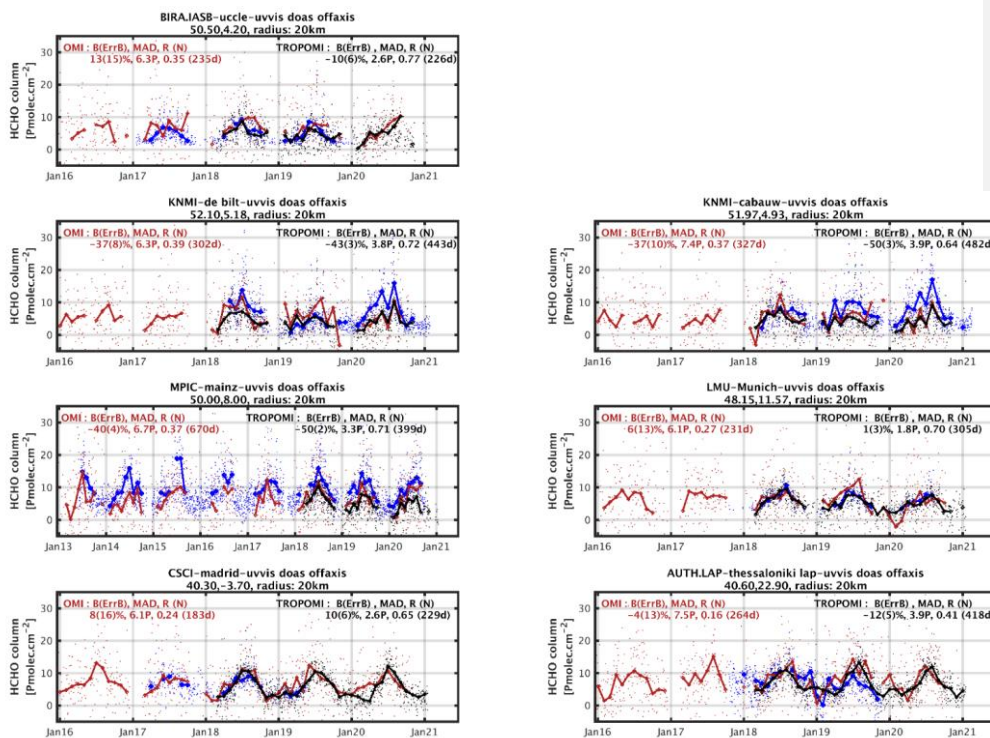
Formatted: Font: 10 pt, Not Bold, Not Italic, Check spelling and grammar

Formatted: Font: 10 pt, Not Bold

Formatted: Font: 10 pt, Not Bold, Not Italic, Check spelling and grammar

Formatted: Font: 10 pt, Not Bold

Formatted: Font: 10 pt, Not Bold, Not Italic, Check spelling and grammar

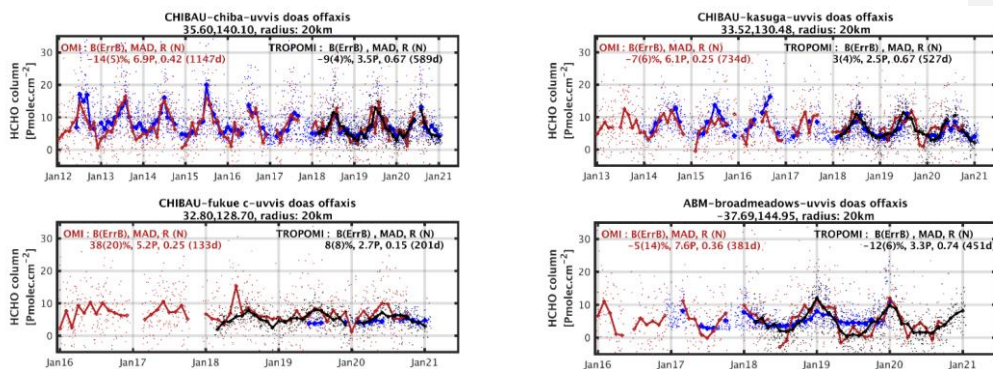


522 Figure 12: Time series of MAX-DOAS HCHO columns (blue), OMI $N_{v,clear}$ (red) and TROPOMI $N_{v,clear}$ (black) at
 523 European sites. Thick lines show monthly median values and dots represent daily median values. Mean relative bias, median
 524 absolute deviations and correlations between the time series are provided for the daily averaged data. [$\text{Pmolec.cm}^{-2} = 10^{15}$
 525 molec.cm^{-2}].

526 In Figure 13, we show three Japanese stations operated by the CHIBA University. Mean HCHO levels in
 527 Japan are comparable to values found at European sites. In Chiba and Kasuga, TROPOMI and MAX-DOAS columns
 528 are strongly correlated (about 0.7), but on the island of Fukue the correlation is poor due to a lack of variability at this
 529 site. At all these sites, TROPOMI shows small biases compared relative to MAX-DOAS data (-9±4% in Chiba, 3±4%
 530 in Kasuga, 8±8% in Fukue). The HCHO observations in Broadmeadows, in Northern Melbourne, have been published
 531 by Ryan et al. (2020). We find a bias of -12±6% for TROPOMI and a good correlation of about 0.7. Quite unusually,
 532 the seasonal amplitude of the MAX-DOAS time series at this station is smaller than observed with OMI and
 533 TROPOMI.

Formatted: Font: 10 pt, Not Bold

Formatted: Font: 10 pt, Not Bold, Not Italic, Check spelling and grammar

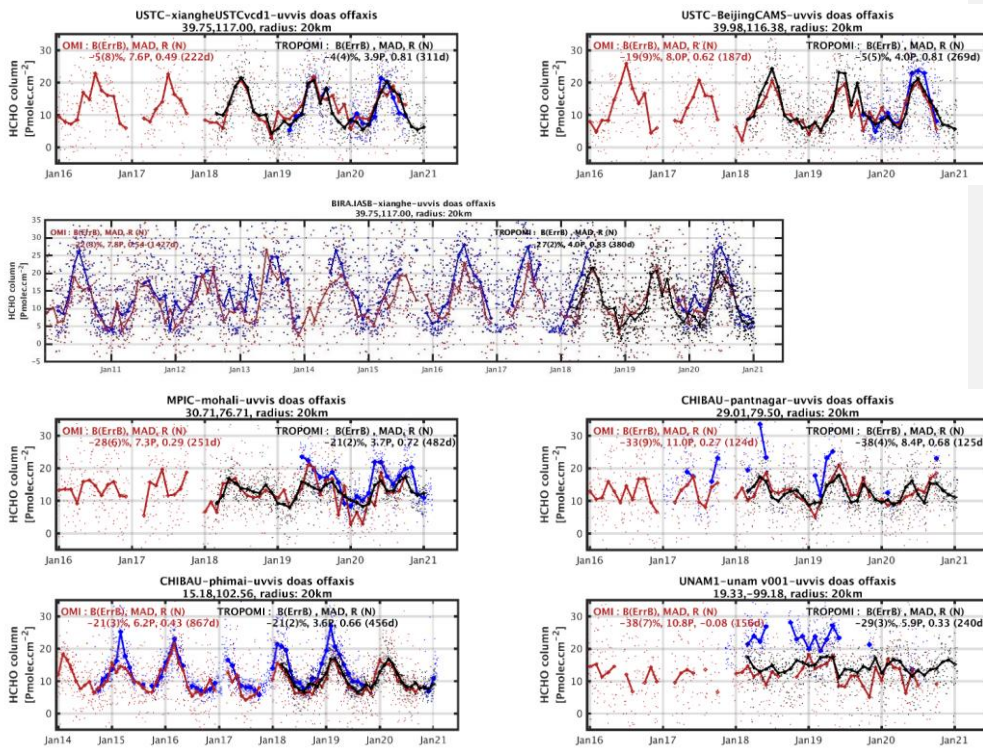


534 Figure 13: Same as Figure 12 in Japan and Australia.

535 Stations with large HCHO levels in China, India, Thailand and Mexico are presented in Figure 14. In China,
 536 we show the results of two instruments in Xianghe, and one instrument in Beijing. With the USTC instruments, we
 537 find small biases of $-4\pm 4\%$ and $-5\pm 5\%$ and correlations larger than 0.8. With the BIRA-IASB instrument in Xianghe,
 538 the correlation is also excellent. The MAX-DOAS columns are larger than the ones obtained with the USTC
 539 instrument, and we find a significant negative bias of the TROPOMI data of $-27\pm 2\%$. However, this larger bias is in
 540 better agreement with the results found for equivalent stations in India and with FTIR validation results in Xianghe
 541 (Vigouroux et al., 2018). This result illustrates the actual uncertainty related to the ground-based measurements
 542 themselves and the need for further harmonisation of the MAX-DOAS network. Correlations in India and Thailand
 543 are of about 0.7, while the biases are consistently negative ($-21\pm 2\%$ in Mohali, $-38\pm 4\%$ in Pantnagar, $-21\pm 2\%$ in
 544 Phimae). The situation is more complex at the UNAM site in Mexico. There, the correlation is poor (0.3), and a
 545 negative bias of $-29\pm 3\%$ is found. These results are however more dependent on the radius considered around the
 546 station, and on the selection of the MAX-DOAS observations (Rivera Cárdenas et al., 2021) (see sect. 5.4).

Formatted: Font: 10 pt, Not Bold

Formatted: Font: 10 pt, Not Bold, Not Italic, Check spelling and grammar



547 Figure 14: Same as Figure 12 at Chinese, Indian, Thailand and Mexican sites.

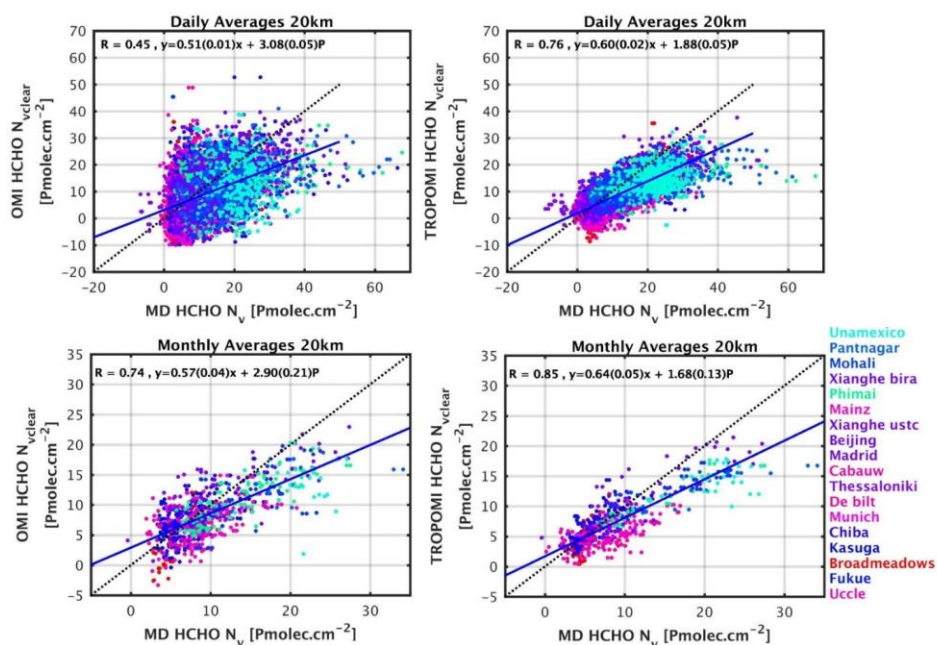
548 Finally, Figure 15 presents scatter plots of the satellite against MAX-DOAS columns, considering all the
 549 stations and for daily and monthly comparisons. Table 3 summarizes the validation results. The best agreement
 550 is found with monthly TROPOMI columns, for which we find a slope of 0.64 and a positive offset of 1.7×10^{15}
 551 molec.cm⁻² compared to the MAX-DOAS columns. Slopes and biases for the large columns are found to be close for
 552 OMI and TROPOMI datasets. The improvement with TROPOMI can be seen in the correlation, offset, and bias values
 553 obtained for the lower columns, as well as in the precision of the daily validation results. On average, the OMI biases
 554 are found to be statistically non-significant for the lowest columns. When considering monthly averaged data, the
 555 correlation between MAX-DOAS and satellite columns improves from 0.74 with OMI to 0.85 with TROPOMI
 556 (+15%). More importantly, it improves from 0.45 to 0.76 when considering daily observations (+68%). The daily
 557 offset is reduced by 60% from OMI to TROPOMI (3.1 to 1.9×10^{15} molec.cm⁻²). In low-emission conditions, the MADs
 558 of the differences provide an upper limit of the precision of the satellite measurements. If we consider HCHO levels
 559 below 8×10^{15} molec.cm⁻² (medium level, but the low range is not represented here), the precision of the daily
 560 TROPOMI HCHO observations is estimated to be 3×10^{15} molec.cm⁻², which represents an improvement of more than
 561 a factor 2 compared to OMI. The precision of monthly TROPOMI observations reaches 1.4×10^{15} molec.cm⁻², which
 562 is close to the Copernicus user requirements.

Formatted: Font: 10 pt, Not Bold

Formatted: Font: 10 pt, Not Bold, Not Italic, Check spelling and grammar

Formatted: Font: 10 pt, Not Bold

Formatted: Font: 10 pt, Not Bold, Not Italic, Check spelling and grammar



563
 564 Figure 15: Scatter plots of OMI (left) and TROPOMI (right) versus MAX-DOAS data for the daily (top) and monthly
 565 (bottom) medians of collocated data. The correlation, slope and intercept of a linear regression using the robust Teil-Shein
 566 estimator is given as inset and plotted as a blue line. The black dotted line is the 1:1 line. The color indicates the latitude of
 567 the station. [Pmolec.cm⁻²=10¹⁵ molec.cm⁻²].

568 Table 3: Summary of validation results for OMI and TROPOMI when considering all collocated pairs (daily or monthly
 569 means) together. Values for HCHO columns lower or larger than 8x10¹⁵ molec.cm⁻² are given in brackets.

	OMI (<, >8x10 ¹⁵ molec.cm ⁻²)	TROPOMI (<, >8x10 ¹⁵ molec.cm ⁻²)
Daily		
MAD [10 ¹⁵ molec.cm ⁻²]	7.3 (6.7, 7.9)	3.8 (3, 4)
Bias+-ErrB [%]	-18±7.5 (-7±12, -21±6.9)	-11±3.6 (-10±4.6, -25±2.8)
Offset [10 ¹⁵ molec.cm ⁻²]	3.1	1.9
Slope	0.51	0.6
Correlation	0.45	0.76
Monthly		
MAD [10 ¹⁵ molec.cm ⁻²]	2.6 (2.5, 3.2)	2.3 (1.4, 2.7)
Bias+-ErrB [%]	-9±13 (9±16.6, -24±12)	-12±8.6 (-5±10, -25±5.7)
Offset [10 ¹⁵ molec.cm ⁻²]	2.9	1.7
Slope	0.57	0.64
Correlation	0.74	0.85

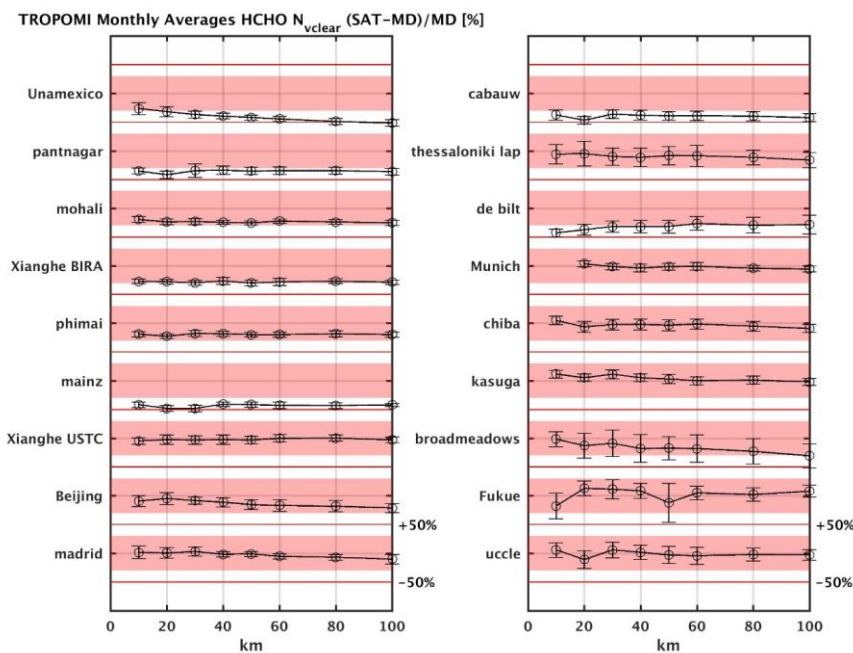
570 **5.2 Sensitivity tests**

571 We performed a few sensitivity tests, in order to evaluate the robustness of the validation results. First, we have used
 572 different radii around the stations (from 10 to 100km), in order to detect possible spatial resolution effects. Results are
 573 presented in [Figure 16](#), for the TROPOMI case. At most stations, the bias shows marginally small
 574 dependency on the radius. Again, this points to the large natural dispersion of the HCHO columns. We find an

Formatted: Font: 10 pt, Not Bold

Formatted: Font: 10 pt, Not Bold, Not Italic, Check spelling and grammar

575 important exception at the UNAM station in Mexico, where the bias clearly increases with the radius (-30% at 10km,
 576 -50% at 100km). At this location, the correlation and MADs are also improved at 10km (not shown). In Beijing and
 577 Broadmeadows, we do observe an increase of the bias at 100km resolution, but the values at 10 and 20km are mostly
 578 equivalent. We performed the same test with OMI, and found consistent results, except that the lower sampling does
 579 not allow using a 10km-radius area.



580
 581 **Figure 16: Median monthly bias as a function of the radius taken around the validation sites. Pink areas indicate 40%**
 582 **bias.**

583 We also evaluated the impact of clouds using two further tests: (1) compare the daily TROPOMI validation results for
 584 N_v and N_{v_clear} , (2) use a much stricter cloud filter on cloud radiance fractions (CRF) of 20% instead of 60%
 585 (equivalent to an effective cloud fraction of 10% instead of 40%). With this strict cloud filter, there is no difference
 586 between N_v and N_{v_clear} . Results are summarized in [Table 4](#). These tests indicate that the TROPOMI HCHO
 587 validation results do not change significantly when a cloud correction is applied, although the N_{v_clear} results are
 588 slightly better. Using a more stringent cloud filter reduces the number of observations. The bias for the lowest columns
 589 becomes positive (from -10 to +3%), and the offset is increased (from 1.9 to 2.6×10^{15} molec. cm^{-2}), while the negative
 590 bias for the largest columns remains equivalent. These numbers will have to be re-evaluated using only the version 2
 591 of the TROPOMI level 2 products available since July 2020, when enough data will be available. However, we note
 592 that this limited impact of the cloud correction on the HCHO columns appears to be consistent with previous satellite

Formatted: Font: 10 pt, Not Bold

593 datasets, independently of the cloud product, as already observed with GOME-2 and OMI, using version 1 of the O2–
 594 O2 cloud product (De Smedt et al., 2015).

595 **Table 4: Summary of daily validation results for TROPOMI when considering all collocated pairs when using N_{v_clear}**
 596 **(first column), (1) when using N_v (second column) or (2) when using a strict cloud filter (third column).**

	TROPOMI N_{v_clear} ($<, >8 \times 10^{15}$ molec.cm $^{-2}$)	TROPOMI N_v ($<, >8 \times 10^{15}$ molec.cm $^{-2}$)	TROPOMI N_{v_clear} CRF<20% ($<, >8 \times 10^{15}$ molec.cm $^{-2}$)
Daily			
MAD [10 15 molec.cm $^{-2}$]	3.8 (3, 4)	3.9 (3, 4.4)	3.3 (2.6, 3.9)
Bias+ErrB [%]	-11±3.6 (-10±4.6, -25±2.8)	-14±3.9 (-12±4.4, -29±2.9)	-3±4.6 (3±6.1, -27±3.8)
Offset [10 15 molec.cm $^{-2}$]	1.9	1.8	2.6
Slope	0.6	0.56	0.57
Correlation	0.76	0.74	0.75

597 **5.3 Effect of vertical smoothing**

598 Three MAX-DOAS stations (Uccle, Xianghe BIRA-IASB, and UNAM) provide retrieved and a priori vertical profiles
 599 together with corresponding averaging kernels ([GEOMS format](#)). This allows taking into account the different vertical
 600 sensitivity of MAX-DOAS and TROPOMI measurements when making comparisons. We follow the methodology
 601 from Rodgers and Connor (2003) described in detail in Vigouroux et al. (2020). It consists of two steps: first taking
 602 into account the different a priori profiles used to retrieve these two data sets (Eq. 2 of Vigouroux et al., 2020), then
 603 smoothing the ground-based profiles using TROPOMI averaging kernels (Eq. 3 of Vigouroux et al., 2020).

604 We give in [Table 5](#) the MAD and biases obtained before and after application of the methodology, for the daily
 605 mean comparisons. Note that the numbers at each site are slightly different than the ones obtained in sect. 5.1 (Figs.
 606 5.3 and 5.5) because the collocated pairs are constructed slightly differently: each collocated pixel of the satellite must
 607 be compared to MAX-DOAS before the daily average because the TROPOMI averaging kernel differs for each pixel.

608 We see in [Table 5](#) that at the cleanest site (Uccle) the effect of the smoothing is small, while at the more
 609 polluted sites Xianghe and UNAM, the biases are strongly reduced by about 20%. This result is in agreement with
 610 previous MAX-DOAS validation studies (De Smedt et al., 2015; Wang et al., 2019b), but also with aircraft and
 611 regional model comparisons (Zhu et al., 2020; Su et al., 2020). The effect of the smoothing is also clearly seen in
 612 [Figure 17](#) where the scatter plots of daily comparisons between TROPOMI and MAX-DOAS are shown
 613 before and after vertical smoothing. The strong effect of the smoothing is usually not observed with FTIR comparisons
 614 because TROPOMI and FTIR measurements have similar vertical sensitivity, which rapidly drops in the atmospheric
 615 layers lower than 3km (Vigouroux et al., 2020), while the MAX-DOAS shows an opposite sensitivity that is maximum
 616 at the surface and generally becomes negligible above 3km (Vigouroux et al., 2008; De Smedt et al., 2015; Wang et
 617 al., 2019a). [An illustration of typical averaging kernels for OMI, TROPOMI and the MAX DOAS instrument in](#)
 618 [Xianghe is provided in Figure S6. As the observation angles and overpass times are very close for OMI and](#)
 619 [TROPOMI, their measurements come with a similar vertical sensitivity.](#) This highlights the importance of taking into
 620 account the different a priori profiles and averaging kernels when comparing techniques having different vertical
 621 sensitivity.

622 **Table 5: Effect of a priori substitution and vertical smoothing on the daily comparisons of TROPOMI and MAX-DOAS**
 623 **data.**

Formatted: Font: 10 pt, Not Bold

Formatted: Font: 10 pt, Not Bold, Not Italic, Check spelling and grammar

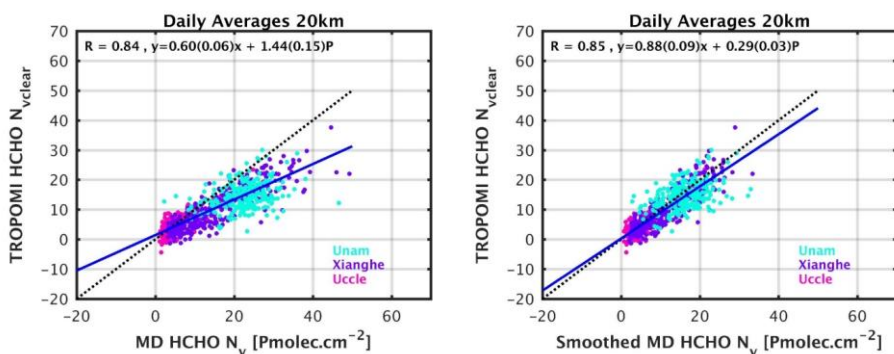
Formatted: Font: 10 pt, Not Bold

Formatted: Font: 10 pt, Not Bold, Not Italic, Check spelling and grammar

Formatted: Font: 10 pt, Not Bold

Formatted: Font: 10 pt, Not Bold, Not Italic, Check spelling and grammar

Daily	Direct comparisons		Rodgers and Connor (2003) applied (a priori substitution and smoothing)	
	MAD [10 ¹⁵ molec.cm ⁻²]	BIAS ± Err_B [%]	MAD [10 ¹⁵ molec.cm ⁻²]	BIAS ± Err_B [%]
Uccle	2.4	-9.4 ± 5.8	2.4	-10.6 ± 5.5
Xianghe, BIRA	3.9	-32.2 ± 2.5	2.7	-9.1 ± 3.0
UNAM	6.1	-34.3 ± 3.2	5.8	-5.8 ± 5.7
	Scatter plot 3 sites		Scatter plot 3 sites	
Offset [10 ¹⁵ molec.cm ⁻²]	1.44		0.29	
Slope	0.60		0.88	
Correlation	0.84		0.85	

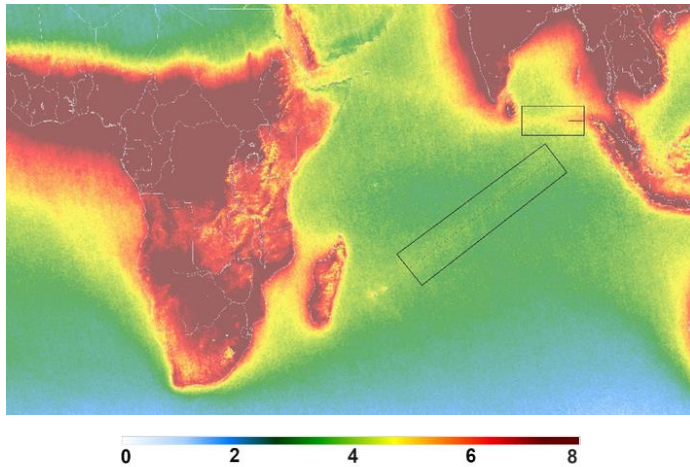


624
625 **Figure 17:** Scatter plots of TROPOMI versus MAX-DOAS data for the daily means of collocated data before (left) and
626 (right) vertical smoothing of the MAX-DOAS profile in Uccle, Xianghe and UNAM/Mexico. The correlation, slope and
627 intercept of a linear regression using the robust Teil-Shein estimator is given inset and plotted as a blue line. The black
628 dotted line is the 1:1 line. [Pmolec.cm⁻²=10¹⁵ molec.cm⁻²].

629 **6 Detection of weak HCHO columns over shipping lanes**

630 As shown above, TROPOMI HCHO observations feature an unprecedented level of precision allowing for an
631 improved detection of small columns at short time scales. Here, we present a case study to illustrate the ability of
632 TROPOMI to detect small HCHO signals related to shipping emissions. When inspecting TROPOMI maps averaged
633 over several months, weak lines of HCHO columns become visible over the background, especially in the Indian
634 Ocean (see e.g. [Figure 5](#)). This becomes even clearer when saturating the continental HCHO columns by
635 setting a lower maximum scale, as in [Figure 18](#), which shows HCHO columns seasonally averaged over the
636 months December, January and February between 2018 and 2021.

- Formatted: Font: 10 pt, Not Bold
- Formatted: Font: 10 pt, Not Bold, Not Italic, Check spelling and grammar
- Formatted: Font: 10 pt, Not Bold
- Formatted: Font: 10 pt, Not Bold, Not Italic, Check spelling and grammar



639 **Figure 18: Seasonal DJF map of TROPOMI HCHO tropospheric columns between Dec. 2018 and Feb.2021, on a spatial**
 640 **grid of 0.05° in latitude and longitude. Observations are only filtered using the provided qa_values >0.5. (max.scale: 8x10¹⁵**
 641 **molec.cm⁻²).**

642 The detection of shipping emissions with satellite observations has often been reported for NO₂ (see for example
 643 Beirle et al., 2004; Richter et al., 2004; 2011; Boersma et al., 2015; Georgoulias et al., 2020), and more recently also
 644 for SO₂ based on OMI measurements (Theys et al., 2015). In the case of HCHO, however, only one study pointed to
 645 the identification of a shipping lane signal detected in a 7-year average of ERS-2 GOME data in the ship track corridor
 646 from Sri Lanka to Singapore (Marbach et al., 2009).

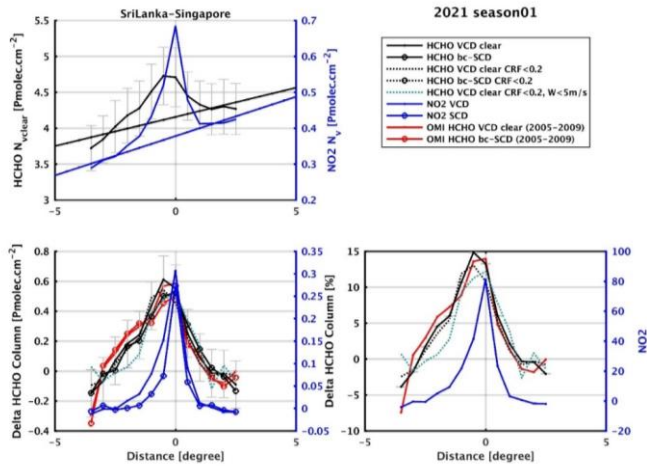
647 Here, we study two lines (1) from Sri Lanka to Singapore and (2) from Madagascar to Singapore. We perform an
 648 analysis and several sensitivity tests in order to gain confidence and information on the enhanced HCHO. As illustrated
 649 in the first panel of [Figure 19](#) (line 1) and [Figure 20](#) (line 2), in each box, we average the HCHO
 650 columns along the ship track to obtain a spatial cross section, and we bin the data as a function of the distance from
 651 the line (distances are expressed in degrees per 0.5° bin). The background level is not constant, for example due to
 652 continental outflow in the Bay of Bengal, and needs to be removed. To do so, we fit a straight line through the column
 653 values at the edges of the box and subtract this line from the signal. This allows to isolate a differential column and to
 654 evaluate its absolute and relative magnitude compared to the background (respectively shown in the second and third
 655 panels of [Figure 19](#) and [Figure 20](#)). For comparison, we perform the same analysis using

656 TROPOMI NO₂ tropospheric columns from the operational product (NO₂ ATBD, Van Geffen et al., 2020). Although
 657 only about half as wide, the localisation of the NO₂ peak is found to be well aligned with the HCHO signal. Along the
 658 line from Sri Lanka to Singapore, we find a similar column enhancement and plume width as in Marbach et al. (2009).

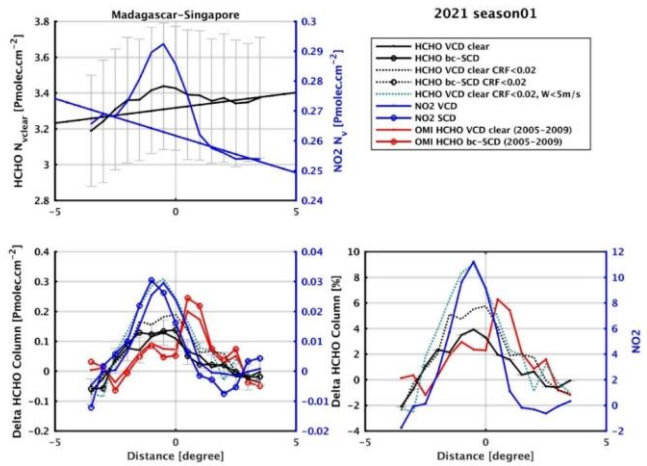
659 In order to exclude a possible indirect AMF effect caused by the TM5 a priori profiles, the same analysis is done based
 660 on background-corrected slant columns (bc-SCD). We also restrict the analysis to clear sky observations, by using a
 661 strict cloud filtering of CRF<20%. Furthermore, we use the wind vector information provided in the TROPOMI L2
 662 product from version 2 onwards (from August 2020), to select only clear-sky observations with low wind conditions

- Formatted: Font: 10 pt, Not Bold
- Formatted: Font: 10 pt, Not Bold, Not Italic, Check spelling and grammar
- Formatted: Font: 10 pt, Not Bold
- Formatted: Font: 10 pt, Not Bold, Not Italic, Check spelling and grammar
- Formatted: Font: 10 pt, Not Bold
- Formatted: Font: 10 pt, Not Bold, Not Italic, Check spelling and grammar
- Formatted: Font: 10 pt, Not Bold
- Formatted: Font: 10 pt, Not Bold, Not Italic, Check spelling and grammar

663 (qa>0.5, CRF<20%, W<5m/s). Finally, we add to the analysis a climatology of HCHO observations based on OMI
 664 measurements (2005-2009).

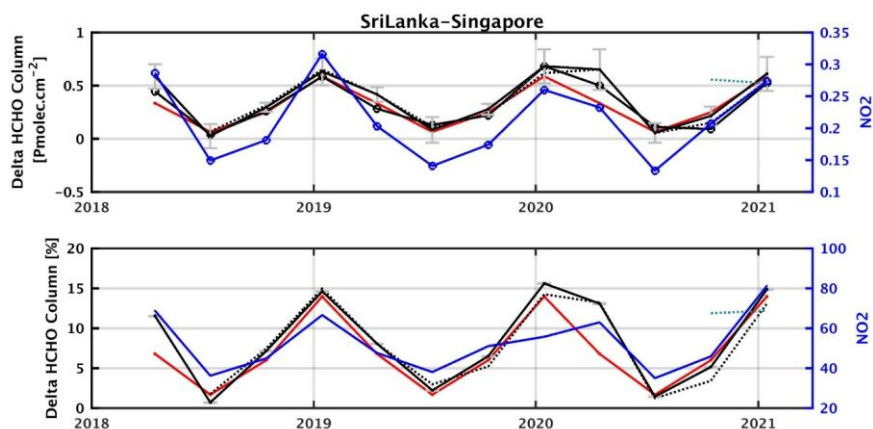


665
 666 **Figure 19: Box average for the first selected line between Sri Lanka and Singapore between Dec. 2020 and Feb. 2021. The**
 667 **x-axis represents the distance (south-north) in degrees from the shipping lane. The first panel shows the HCHO (in black)**
 668 **and NO₂ (in blue) tropospheric columns, binned per distance from the line center. The fitted lines are used to remove the**
 669 **background contribution. The two bottom panels present the absolute (left) and relative (right) column deviations from**
 670 **the background line. The analysis is performed on the slant and the vertical columns (circles/lines), using a stricter cloud**
 671 **filtering (CRF<20%, black dotted line), an additional filter on the wind velocity (W<5m/s, green dotted line), and finally on**
 672 **OMI observations averaged between 2005 and 2009 (red). [Pmolec.cm⁻² = 1x10¹⁵ molec.cm⁻²].**



673
 674 **Figure 20: Same as Figure 19 for the second selected line between Madagascar and Singapore.**

675 Using this approach, we analysed HCHO datasets for each season between MAM 2018 and DJF 2021. The absolute
 676 and relative magnitude of the largest detected signal is plotted as a function of the season in [Figure 21](#) and
 677 [Figure 22](#). Along the two lines, the signal is detected in the slant columns of HCHO and NO₂ as well. This
 678 excludes the possibility of an artefact coming from the TM5 a priori profiles. The signal remains detectable in clear-
 679 sky observations, and is even increased along the second line. We observe a similar effect of the wind speed filtering
 680 (last two seasons). Selecting only low-wind conditions clearly enhances the signal along line 2, and during SON along
 681 line 1. The magnitude of the detected HCHO signal is larger along line 1 (from 0.2 to 0.7x10¹⁵ molec.cm⁻², 15%)
 682 compared to line 2 (from 0.1 to 0.3x10¹⁵ molec.cm⁻², 8%). We find that the absolute magnitude of the HCHO signal
 683 is larger than the NO₂ signal by a factor of 3 to 10, but the relative increase of the NO₂ columns is significantly larger:
 684 60% along line 1 and 15% along line 2. Both lines show a clear seasonality, particularly in the HCHO columns, with
 685 a maximum during the DJF seasons seen in the OMI climatology and in the TROPOMI 3-months averages. The
 686 HCHO signal presents a clear drop in JJA along line 1. This is related to the wind direction and strength, which bring
 687 the line signal closer to the HCHO continental outflow, making its detection more difficult. The OMI data need to be
 688 averaged over several years in order to detect a significant signal. While the first line is well detected in the 5-years
 689 OMI climatology, the second line presents a smaller magnitude, a larger variability, and cannot be detected in the
 690 most recent years of OMI measurements.



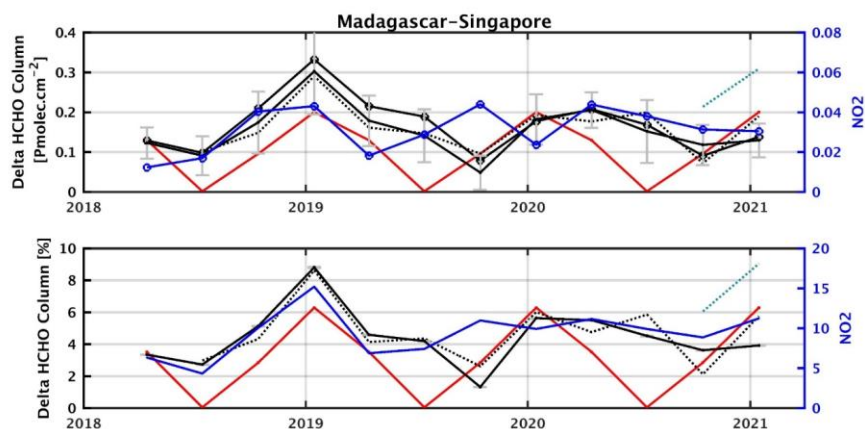
691
 692 **Figure 21:** Seasonal variation of the absolute (top panel) and relative (center panel) column deviations of the TROPOMI
 693 HCHO (black), OMI 2005-2009 climatology HCHO (red) and TROPOMI NO₂ (blue) tropospheric columns along the Sri
 694 Lanka - Singapore line. For each season, the maximum deviation compared to the background is provided. The results of
 695 the analysis are given for the slant and the vertical columns (circles/lines), using a stricter cloud filtering (CRF<20%, black
 696 dotted line), an additional filter on the wind velocity (W<5m/s, green dotted line). [Pmolec.cm⁻² = 1x10¹⁵ molec.cm⁻²].

Formatted: Font: 10 pt, Not Bold

Formatted: Font: 10 pt, Not Bold, Not Italic, Check spelling and grammar

Formatted: Font: 10 pt, Not Bold

Formatted: Font: 10 pt, Not Bold, Not Italic, Check spelling and grammar



697

698 Figure 22: Same as Figure 21 along the Madagascar – Singapore line.

699 Using TROPOMI HCHO observations averaged over 3 months, it is therefore possible to detect a signal as small as
 700 0.1×10^{15} molec. cm^{-2} (with a median deviation of 0.03×10^{15} molec. cm^{-2}), after removal of the background contribution.

701 Note that along the first line a similar analysis can also be performed on a monthly basis. While we show several
 702 evidences that the signal is related to shipping emissions, its source is not studied here. As discussed in Marbach et al.
 703 (2009) it could be due to secondary HCHO production via the atmospheric oxidation of NMVOCs emitted from ship
 704 engines but also to enhanced CH_4 oxidation by elevated levels of OH radicals within the ship plumes. Model analysis
 705 suggests that the second hypothesis is the main factor responsible for the elevated HCHO levels (Song et al., 2010).

706 Other HCHO lines can be detected as well in the Tropics, although weaker in magnitude or closer to the continental
 707 outflow (in the South-West of Africa or in the West of India). More advanced techniques to separate the signal from
 708 the background and to account for wind dispersion effects could help in detecting more shipping lanes but also weak
 709 continental emissions (Beirle et al., 2004).

710 7 Conclusions

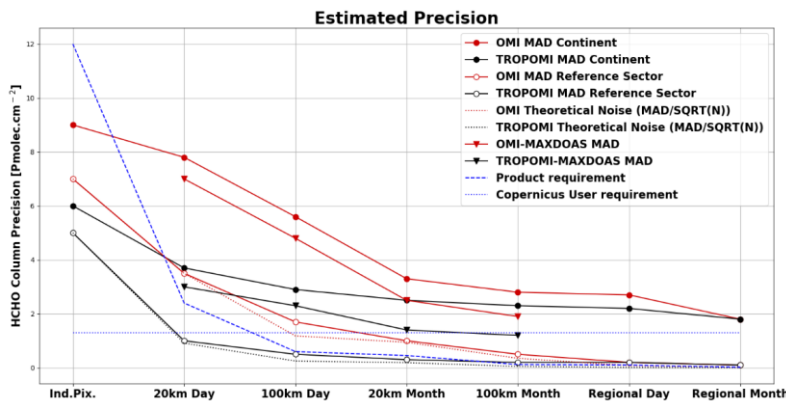
711 Owing to its high spatial resolution resulting in many measurement points, coupled with an improved signal to noise
 712 ratio at single pixel level, TROPOMI allows to monitor HCHO tropospheric columns from space with an
 713 unprecedented definition. The global and regional maps show a clear reduction of the noise compared to previous
 714 sensors, allowing for the detection of weaker HCHO signals, and the monitoring of HCHO variations on a much
 715 shorter time scale.

716 We have evaluated the TROPOMI HCHO operational product against the QA4ECV OMI HCHO dataset, and against
 717 a network of 18 ground-based MAX-DOAS instruments. The gain in precision at different spatial and temporal scales
 718 was estimated by (1) comparing the median deviation of the averaged columns, and (2) validating the data using
 719 MAX-DOAS column network measurements. Both methods include additional noise components from temporal

720 variation, spatial variation and ground-based column precision. Results are summarized in [Figure 23](#) where
 721 precision estimates are provided for observations over regions with enhanced continental emissions and for
 722 background conditions, as a function of the time resolution (daily or monthly averages) and of the spatial resolution
 723 (from 20km to regional scale). At 20 and 100km resolution, both the median deviation approach and the validation
 724 results lead to very consistent estimates of the precision. The theoretical noise is also represented in the figure; it
 725 decreases as the squared root of the number of observations included in the averages. In remote conditions, the median
 726 deviation of the averaged columns follows closely the theoretical noise until reaching a threshold. If we consider a
 727 large region in the reference sector, all estimates converge towards a limit of about $0.2 \times 10^{15} \text{ molec.cm}^{-2}$
 728 (day) to $0.1 \times 10^{15} \text{ molec.cm}^{-2}$ (month) both for OMI and TROPOMI. Over continental emission sources, the reduction
 729 of the noise is counterbalanced by the HCHO natural variability and by other sources of pseudo-noise which depend
 730 on the spatial and temporal scales of the observations. The largest improvement brought by TROPOMI is found for
 731 daily observations at 20km resolution, for which a gain in precision by a factor of 3 is obtained compared to OMI.
 732 The product and COPERNICUS user requirements for precision are also represented in the figure. Both are reached
 733 with TROPOMI using daily averaged data at the resolution of 20km if we consider the dispersion in remote regions.
 734 However, over continental emissions, local variability effects added up to the estimated precision that reaches a
 735 threshold of about $2 \times 10^{15} \text{ molec.cm}^{-2}$.

Formatted: Font: 10 pt, Not Bold

Formatted: Font: 10 pt, Not Bold, Not Italic, Check spelling and grammar



736
 737 Figure 23: Estimated precision of OMI (in red) and TROPOMI (in black) HCHO columns at different spatial and temporal
 738 scales (20km, 100km, regions, day/month). The median deviation of the satellite HCHO columns are provided for
 739 continental emissions (plain circles) and in the remote reference sector (white circles). Validation estimates are plotted at
 740 20km and 100km (MAD of differences between satellite and MAX-DOAS columns, triangles). The theoretical noise (dotted
 741 lines) corresponds to single measurement precision divided by the square root of observations. The dashed blue line is the
 742 TROPOMI product requirement, based on a single measurement precision of $12 \times 10^{15} \text{ molec.cm}^{-2}$. The horizontal blue line
 743 at $1.3 \times 10^{15} \text{ molec.cm}^{-2}$ represents the COPERNICUS user requirement. [$\text{Pmolec.cm}^{-2} = 1 \times 10^{15} \text{ molec.cm}^{-2}$].

744 For the HCHO absolute values, we show that OMI and TROPOMI observations agree very well for moderate to large
 745 HCHO levels (columns larger than $5 \times 10^{15} \text{ molec.cm}^{-2}$) for which the bias between both datasets is smaller than 10%.
 746 For lower columns however, OMI observations present a remaining bias of about +20% compared to TROPOMI. This
 747 good agreement is obtained by considering vertical columns calculated with air mass factors not corrected for cloud

748 effects (clear VCD). This allows to avoid biases related to differences in the cloud products. For all applications that
749 require combining the OMI and TROPOMI observations for low to moderate cloud fractions, we therefore advise to
750 use clear VCDs. Validation results confirm the good agreement between the OMI and TROPOMI datasets and a
751 similar underestimation of both products in the highest range of the HCHO levels (-25% in average for columns larger
752 than 8×10^{15} molec.cm⁻²). For medium columns, OMI presents a slight overestimation compared to MAX-DOAS data,
753 which is not observed for TROPOMI. Sensitivity tests show that validation results obtained with the TROPOMI
754 HCHO columns are weakly dependent on the cloud correction. They also depend weakly on the radius considered
755 around the station, with a few exceptions such as Mexico city or coastal stations. On the contrary, the vertical
756 smoothing (tested at three stations) has a strong effect on the comparison with MAX-DOAS. After taking into account
757 the different a priori profiles and averaging kernels, the bias for large HCHO columns is strongly reduced by about
758 20%.

759 Comparing OMI and TROPOMI monthly averaged HCHO columns, we do not observe significant differences related
760 to the spatial resolution, except in regions surrounded by natural boundaries where the benefit of the finer spatial
761 resolution of TROPOMI is clearly apparent. The weak sensitivity to the spatial resolution of HCHO measurements
762 can be understood when considering that HCHO is a secondary product from the degradation of NMOVCs with
763 various lifetimes, which results in a general spread of the HCHO spatial distributions. The large number of TROPOMI
764 observations allows to perform validation at a resolution as small as 10km on a daily basis with a sufficient precision,
765 which is not possible with OMI. It is clear that TROPOMI brings a significant improvement in the temporal resolution
766 of the observations. At most of the validation sites, TROPOMI allows for daily validation results as robust as those
767 obtained with OMI on a monthly basis.

768 The number of ground-based stations providing MAX-DOAS HCHO observations is constantly growing, providing
769 a large range of observation conditions, and for some of them, over several years allowing the comparisons of the
770 performances of several satellite datasets. Note however that the lower range of HCHO levels is under-represented,
771 as well as some of the largest emission regions such as South America or Africa. Following the validation study of
772 Vigouroux et al. (2020) based on a FTIR network of instruments, this study illustrates again the added value of using
773 a large network of instruments to draw more robust conclusions. FTIR and MAX-DOAS networks are complementary
774 to each other and could be combined to cover as many conditions as possible. Similarly to what was achieved for the
775 FTIR network, the MAX-DOAS HCHO datasets would benefit from further homogenisation efforts.

776 Finally, to illustrate the benefit of TROPOMI for the detection of small HCHO signals, we present a case study
777 addressing the detection of shipping lanes in the Indian Ocean. Using simultaneous observations of tropospheric NO₂
778 and meteorological wind field data, we present strong evidences for an HCHO production in regions affected by
779 shipping emissions. Owing to the [fine spatial resolution and high spatial sampling sensitivity](#) of TROPOMI, such small
780 signals can now be observed from space on a seasonal basis.

781 **Code and data availability**

782 The S5p HCHO data are available at <https://scihub.copernicus.eu>. The access and use of any Copernicus Sentinel data available
783 through the Copernicus Sentinel Data Hub is governed by the Legal Notice on the use of Copernicus Sentinel Data and Service
784 Information and is given here: https://sentinels.copernicus.eu/documents/247904/690755/Sentinel_Data_Legal_Notice.
785 The QA4ECV OMI HCHO product is available at <https://doi.org/10.18758/71021031> (De Smedt et al., 2017). The MAX-DOAS
786 datasets can be requested from the individual PIs of each station.

787 **Author contributions**

788 IDS coordinated the paper and carried out the analysis. GP and CV are PIs of the NIDFORVAL S5PVT project, SC ensures the
789 MPC routine validation. IDS, PH, YH, Cle, DL, FR, NT, JV, MVR developed the TROPOMI HCHO product. FB, IDS, YH, AR,
790 MVR, TW developed the QA4ECV OMI HCHO product. AB, NB, KLC, SD, FH, HI, VK, CLi, AP, CRC, RGR, MVR, TW are
791 PIs for the QA4ECV MAX-DOAS measurements. BL, SC, GP, CV performed MAX-DOAS data collection and format
792 harmonization and carried out the validation analysis. SC, KUE and JCL are responsible of the MPC routine validation. MVR is
793 the coordinator of this research. All co-authors revised and commented on the paper.

794 **Acknowledgements**

795 This work contains modified Copernicus Sentinel-5 Precursor satellite data (2018-2020) post-processed by BIRA-IASB. Part of
796 the reported work was carried out in the framework of the Copernicus Sentinel-5 Precursor Mission Performance Centre (S5p
797 MPC), contracted by the European Space Agency (ESA/ESRIN, Contract No. 4000117151/16/I-LG) and supported by the Belgian
798 Federal Science Policy Office (BELSPO), the Royal Belgian Institute for Space Aeronomy (BIRA-IASB) and the German
799 Aerospace Centre (DLR). BIRA-IASB acknowledges national funding from BELSPO and ESA through the ProDEX projects
800 TRACE-S5P (TRACE-S5P project) and TROVA. Part of this work was carried out also in the framework of the S5p Validation
801 Team (S5PVT) AO projects NIDFORVAL (ID #28607, PI G. Pinardi, C. Vigouroux, BIRA-IASB). Multi-sensor HCHO
802 developments have been funded by the EU FP7 QA4ECV project (grant no. 607405), in close cooperation with KNMI, University
803 of Bremen, MPIC-Mainz and WUR. Work by H. Irie was supported by the Environment Research and Technology Development
804 Fund (JPMEERF20192001 and JPMEERF20215005) of the Environmental Restoration and Conservation Agency of Japan, JSPS
805 KAKENHI (grant numbers JP19H04235 and JP20H04320), and the JAXA 2nd research announcement on the Earth Observations
806 (grant number 19RT000351). We acknowledge Mark Wenig from LMU for supporting the MAX-DOAS operations in Munich,
807 Caroline Fayt and Christian Herman from BIRA-IASB for the Uccle and Xianghe instruments, as well as Pucāi Wang from
808 IAP/CAS for maintaining the BIRA-IASB instrument in Xianghe. We thank Alejandro Bezanilla from CCA-UNAM, Manish Naia
809 from ARIES for the MAX-DOAS instrument operation in Pantnager and Thanawat Jarupongsakul from Chulalongkorn University
810 for the Phimai station. We acknowledge IISER Mohali Atmospheric Chemistry Facility for supporting the MAX-DOAS operations
811 in Mohali.

812 **References**

813 Alvarado, L. M. A., Richter, A., Vrekoussis, M., Hilboll, A., Kalisz Hedegaard, A. B., Schneising, O., and Burrows,
814 J. P.: Unexpected long-range transport of glyoxal and formaldehyde observed from the Copernicus Sentinel-5

815 Precursor satellite during the 2018 Canadian wildfires, *Atmos. Chem. Phys.*, 20, 2057–2072,
816 <https://doi.org/10.5194/acp-20-2057-2020>, 2020.

817 Arellano, J., Krüger, A., Rivera, C., Stremme, W., Friedrich, M., Bezanilla, A., and Grutter, M.: The MAX-DOAS
818 network in Mexico City to measure atmospheric pollutants, *Atmosfera*, 29,157–167,
819 <https://doi.org/10.20937/ATM.2016.29.02.05>, 2016.

820 Barkley, M. P., González Abad, G., Kurosu, P. T., Spurr, R., Torbatian, S. and Lerot, C.: OMI air-quality monitoring
821 over the Middle East, *Atmos. Chem. Phys.*, 17(7), 4687–4709, doi:10.5194/acp-17-4687-2017, 2017.

822 Bauwens, M., Stavrou, T., Müller, J.-F., De Smedt, I., Van Roozendael, M., van der Werf, G. R., Wiedinmyer, C.,
823 Kaiser, J. W., Sindelarova, K., and Guenther, A.: Nine years of global hydrocarbon emissions based on source
824 inversion of OMI formaldehyde observations, *Atmos. Chem. Phys.*, 16, 10133–10158, [https://doi.org/10.5194/acp-](https://doi.org/10.5194/acp-16-10133-2016)
825 [16-10133-2016](https://doi.org/10.5194/acp-16-10133-2016), 2016.

826 Beirle, S., Platt, U., von Glasow, R., Wenig, M., and Wagner, T. : Estimate of nitrogen oxide emissions from shipping
827 by satellite remote sensing, *Geophys. Res. Lett.*, 31, L18102, doi:10.1029/2004GL020312, 2004.

828 Beirle, S., Borger, C., Dörner, S., Li, A., Hu, Z., Liu, F., Wang, Y. and Wagner, T.: Pinpointing nitrogen oxide
829 emissions from space, *Sci. Adv.*, 5(11), eaax9800, doi:10.1126/sciadv.aax9800, 2019.

830 Benavent, N., Garcia-Nieto, D., Wang, S. and Saiz-Lopez, A.: MAX-DOAS measurements and vertical profiles of
831 glyoxal and formaldehyde in Madrid, Spain, *Atmos. Environ.*, 199, 357–367,
832 doi:<https://doi.org/10.1016/j.atmosenv.2018.11.047>, 2019.

833 Boersma, K. F., Eskes, H. J., and Brinksma, E. J.: Error analysis for tropospheric NO₂ retrieval from space, *J.*
834 *Geophys. Res.*, 109, <https://doi.org/10.1029/2003JD003962>, 2004.

835 Boersma, K. F., Vinken, G. C. M. and Tournadre, J.: Ships going slow in reducing their NO_x emissions: changes in
836 2005–2012 ship exhaust inferred from satellite measurements over Europe, *Environ. Res. Lett.*, 10(7), 074007,
837 doi:10.1088/1748-9326/10/7/074007, 2015.

838 Boersma, K. F., Eskes, H. J., Richter, A., Smedt, I. De, Lorente, A., Beirle, S., Van Geffen, J. H. G. M., Zara, M.,
839 Peters, E., Roozendael, M. Van and others: Improving algorithms and uncertainty estimates for satellite NO₂
840 retrievals: results from the quality assurance for the essential climate variables (QA4ECV) project, *Atmos. Meas.*
841 *Tech.*, 11(12), 6651–6678, 2018.

842 Bösch, T., Rozanov, V., Richter, A., Peters, E., Rozanov, A., Wittrock, F., Merlaud, A., Lampel, J., Schmitt, S., de
843 Haij, M., 20Berkhout, S., Henzing, B., Apituley, A., den Hoed, M., Vonk, J., Tiefengraber, M., Müller, M.,
844 and Burrows, J. P.: BOREAS –a new MAX-DOAS profile retrieval algorithm for aerosols and trace gases, *Atmos.*
845 *Meas. Tech.*, 11, 6833–6859, <https://doi.org/10.5194/amt-11-6833-2018>, 2018.

846 Bovensmann, H., Peuch, V.-H., van Weele, M., Erbertseder, T., and Veihelmann, B.: Report Of The Review Of User
847 Requirements For Sentinels-4/-5, ESA, EOP-SM/2281/BV-bv, issue: 1.2, 2011.

848 Brinksma, E. J., Pinardi, G., Volten, H., Braak, R., Richter, A., Scho, A., Van Roozendael, M., Fayt, C., Hermans, C.,
849 Dirksen, R. J., Vlemmix, T., Berkhout, A. J. C., Swart, D. P. J., Oetjen, H., Wittrock, F., Wagner, T., Ibrahim, O. W.,
850 Leeuw, G. De, Moerman, M., Curier, R. L., Celarier, E. A., Cede, A., Knap, W. H., Veeffkind, J. P., Eskes, H. J.,
851 Allaart, M., Rothe, R., PETERS, A. and Levelt, P. F.: The 2005 and 2006 DANDELIONS NO₂ and aerosol
852 intercomparison campaigns, *J. Geophys. Res.*, 113(D16), 1–18, doi:10.1029/2007JD008808, 2008.

853 Cao, H., Fu, T.-M., Zhang, L., Henze, D. K., Miller, C. C., Lerot, C., Abad, G. G., Smedt, I. De, Zhang, Q.,
854 Roozendael, M. van and others: Adjoint inversion of Chinese non-methane volatile organic compound emissions using
855 space-based observations of formaldehyde and glyoxal, *Atmos. Chem. Phys.*, 18(20), 15017–15046, 2018.

856 Chan, K. L., Wang, Z., Ding, A., Heue, K.-P., Shen, Y., Wang, J., Zhang, F., Shi, Y., Hao, N., and Wenig, M.: MAX-
857 DOAS measurements of tropospheric NO₂ and HCHO in Nanjing and a comparison to ozone monitoring instrument
858 observations, *Atmos. Chem. Phys.*, 19, 10051–10071, <https://doi.org/10.5194/acp-19-10051-2019>, 2019.

859 Chan, K. L., Wiegner, M., van Geffen, J., De Smedt, I., Alberti, C., Cheng, Z., Ye, S., and Wenig, M.: MAX-DOAS
860 measurements of tropospheric NO₂ and HCHO in Munich and the comparison to OMI and TROPOMI satellite
861 observations, *Atmos. Meas. Tech.*, 13, 4499–4520, <https://doi.org/10.5194/amt-13-4499-2020>, 2020.

862 Chance, K. V., Palmer, P. I., Martin, R. V., Spurr, R. J. D., Kurosu, T. P. and Jacob, D. J.: Satellite observations of
863 formaldehyde over North America from GOME, *Geophysical Research Letters*, 27(21), 3461–3464,
864 doi:10.1029/2000GL011857, 2000.

865 Chan Miller, C., Jacob, D. J., Marais, E. A., Yu, K., Travis, K. R., Kim, P. S., Fisher, J. A., Zhu, L., Wolfe, G. M.,
866 Hanisco, T. F., Keutsch, F. N., Kaiser, J., Min, K.-E., Brown, S. S., Washenfelder, R. A., González Abad, G., and
867 Chance, K.: Glyoxal yield from isoprene oxidation and relation to formaldehyde: chemical mechanism, constraints
868 from SENEX aircraft observations, and interpretation of OMI satellite data, *Atmos. Chem. Phys.*, 17, 8725–8738,
869 <https://doi.org/10.5194/acp-17-8725-2017>, 2017.

870 Choi, Y. and Souri, A. H.: Seasonal behavior and long-term trends of tropospheric ozone, its precursors and chemical
871 conditions over Iran: A view from space, *Atmos. Environ.*, 106, 232–240,
872 doi:<https://doi.org/10.1016/j.atmosenv.2015.02.012>, 2015.

873 Clémer, K., Van Roozendael, M., Fayt, C., Hendrick, F., Hermans, C., Pinardi, G., Spurr, R., Wang, P. and De
874 Mazière, M.: Multiple wavelength retrieval of tropospheric aerosol optical properties from MAX-DOAS
875 measurements in Beijing, *Atmos. Meas. Tech.*, 3, 863–878 [online] Available from: doi:10.5194/amt-3-863-2010,
876 2010.

877 Compernelle, S., Argyrouli, A., Lutz, R., Sneep, M., Lambert, J.-C., Fjæraa, A. M., Hubert, D., Keppens, A., Loyola,
878 D., O'Connor, E., Romahn, F., Stammes, P., Verhoelst, T. and Wang, P.: Validation of the Sentinel-5 Precursor
879 TROPOMI cloud data with Cloudnet, Aura OMI O₂-O₂, MODIS and Suomi-NPP VIIRS, *Atmos. Meas. Tech.*
880 *Discuss.*, (June), 1–33, doi:10.5194/amt-2020-122, 2020.

881 De Smedt, I., Müller, J.-F., Stavrou, T., van der A, R., Eskes, H. and Van Roozendael, M.: Twelve years of global
882 observations of formaldehyde in the troposphere using GOME and SCIAMACHY sensors, *Atmos. Chem. Phys.*,
883 8(16), 4947-4963, 2008.

884 De Smedt, I., Stavrou, T., Müller, J. F., van Der A, R. J. and Van Roozendael, M.: Trend detection in satellite
885 observations of formaldehyde tropospheric columns, *Geophys. Res. Lett.*, 37(18), L18808,
886 doi:10.1029/2010GL044245, 2010.

887 [De Smedt, I., Van Roozendael, M., Stavrou, T., Müller, J.-F., Lerot, C., Theys, N., Valks, P., Hao, N., and van der](#)
888 [A. R.: Improved retrieval of global tropospheric formaldehyde columns from GOME-2/MetOp-A addressing noise](#)
889 [reduction and instrumental degradation issues, *Atmos. Meas. Tech.*, 5, 2933–2949, \[https://doi.org/10.5194/amt-5-\]\(https://doi.org/10.5194/amt-5-2933-2012\)](#)
890 [2933-2012, 2012.](#) [De Smedt, I., Van Roozendael, M., Stavrou, T., Müller, J. F., Lerot, C., Theys, N., Valks, P.,](#)
891 [Hao, N., and van der A, R.: Improved retrieval of global tropospheric formaldehyde columns from GOME-2/MetOp-](#)
892 [A addressing noise reduction and instrumental degradation issues, *Atmos. Meas. Tech. Discuss.*, 5, 5571–5616,](#)
893 [doi:10.5194/amt-d-5-5571-2012, Special Issue: GOME-2: calibration, algorithms, data products and validation, 2012.](#)

894 De Smedt, I., Stavrou, T., Hendrick, F., Danckaert, T., Vlemmix, T., Pinardi, G., Theys, N., Lerot, C., Gielen, C.,
895 Vigouroux, C., Hermans, C., Fayt, C., Veefkind, P., Müller, J.-F., and Van Roozendael, M.: Diurnal, seasonal and
896 long-term variations of global formaldehyde columns inferred from combined OMI and GOME-2 observations,
897 *Atmos. Chem. Phys.*, 15, 12519-12545, doi:10.5194/acp-15-12519-2015, 2015

898 De Smedt, I., Yu, H., Richter, A., Beirle, S., Eskes, H., Boersma, K.F., Van Roozendael, M., Van Geffen, J., Lorente,
899 A. and Peters, E.: QA4ECV HCHO tropospheric column data from OMI (Version 1.1) [Data set], 2017.

900 De Smedt, I., Theys, N., Yu, H., Danckaert, T., Lerot, C., Compennolle, S., Van Roozendael, M., Richter, A., Hilboll,
901 A., Peters, E., Pedernana, M., Loyola, D., Beirle, S., Wagner, T., Eskes, H., van Geffen, J., Boersma, K. F., and
902 Veefkind, P.: Algorithm theoretical baseline for formaldehyde retrievals from S5P TROPOMI and from the QA4ECV
903 project, *Atmos. Meas. Tech.*, 11, 2395–2426, <https://doi.org/10.5194/amt-11-2395-2018>, 2018.

904 Dimitropoulou, E., Hendrick, F., Pinardi, G., Friedrich, M. M., Merlaud, A., Tack, F., De Longueville, H., Fayt, C.,
905 Hermans, C., Laffineur, Q., Fierens, F., and Van Roozendael, M.: Validation of TROPOMI tropospheric NO₂ columns
906 using dual-scan multi-axis differential optical absorption spectroscopy (MAX-DOAS) measurements in Uccle,
907 Brussels, *Atmos. Meas. Tech.*, 13, 5165–5191, <https://doi.org/10.5194/amt-13-5165-2020>, 2020.

908 Drosoglou, T., Bais, A. F., Zyrichidou, I., Kouremeti, N., Poupkou, A., Liora, N., Giannaros, C., Koukouli, M. E.,
909 Balis, D., and Melas, D.: Comparisons of ground-based tropospheric NO₂ MAX-DOAS measurements to satellite
910 observations with the aid of an air quality model over the Thessaloniki area, Greece, *Atmos. Chem. Phys.*, 17, 5829-
911 5849, <https://doi.org/10.5194/acp-17-5829-2017>, 2017.

912 ESA: Sentinel-5 Precursor Calibration and Validation Plan for the Operational Phase, ref: ESA-EOPG-CSCOP-PL-
913 0073, issue:1.1, 06/11/2017 ([https://sentinel.esa.int/documents/247904/2474724/Sentinel-5P-Calibration-and-](https://sentinel.esa.int/documents/247904/2474724/Sentinel-5P-Calibration-and-Validation-Plan.pdf)
914 [Validation-Plan.pdf](https://sentinel.esa.int/documents/247904/2474724/Sentinel-5P-Calibration-and-Validation-Plan.pdf)).

915 [Fortems-Cheiney, A., Chevallier, F., Pison, I., Bousquet, P., Saunois, M., Szopa, S., Cressot, C., Kurosu, T. P., Chance,](#)
916 [K., and Fried, A.: The formaldehyde budget as seen by a global-scale multi-constraint and multi-species inversion](#)
917 [system, *Atmos. Chem. Phys.*, 12, 6699–6721, <https://doi.org/10.5194/acp-12-6699-2012>, 2012](#)~~Fortems-Cheiney, A.,~~
918 ~~Chevallier, F., Pison, I., Bousquet, P., Saunois, M., Szopa, S., Cressot, C., Kurosu, T. P., Chance, K. and Fried, A.:~~
919 ~~The formaldehyde budget as seen by a global-scale multi-constraint and multi-species inversion system, *Atmos-*~~
920 ~~*Chem. Phys. Discuss.*, 12(3), 6909–6955, [doi:10.5194/acpd-12-6909-2012](https://doi.org/10.5194/acpd-12-6909-2012), 2012.~~

921 Franco, B., Hendrick, F., Van Roozendaal, M., Müller, J.-F., Stavrou, T., Marais, E. A., Bovy, B., Bader, W., Fayt,
922 C., Hermans, C., Lejeune, B., Pinardi, G., Servais, C., and Mahieu, E.: Retrievals of formaldehyde from ground-based
923 FTIR and MAX-DOAS observations at the Jungfraujoch station and comparisons with GEOS-Chem and IMAGES
924 model simulations, *Atmos. Meas. Tech.*, 8, 1733–1756, [doi:10.5194/amt-8-1733-2015](https://doi.org/10.5194/amt-8-1733-2015), 2015.

925 Franco, B., Blumenstock, T., Cho, C., Clarisse, L., Clerbaux, C., Coheur, P.-F., De Mazière, M., De Smedt, I., Dorn,
926 H.-P., Emmerichs, T., Fuchs, H., Gkatzelis, G., Griffith, D., et al.: Ubiquitous atmospheric production of organic acids
927 mediated by warm clouds, *Nature*, 2017-10-14339, 2021.

928 Friedrich, M. M., Rivera, C., Stremme, W., Ojeda, Z., Arellano, J., Bezanilla, A., García-Reynoso, J. A., and Grutter,
929 M.: NO₂ vertical profiles and column densities from MAX-DOAS measurements in Mexico City, *Atmos. Meas.*
930 *Tech.*, 12, 2545–2565, <https://doi.org/10.5194/amt-12-2545-2019>, 2019.

931 Frieß, U., Monks, P. S., Remedios, J. J., Rozanov, A., Sinreich, R., Wagner, T. and Platt, U.: MAX-DOAS O₄
932 measurements: A new technique to derive information on atmospheric aerosols: 2. Modeling studies, *J. Geophys. Res.*,
933 111(D14), [doi:10.1029/2005JD006618](https://doi.org/10.1029/2005JD006618), 2006.

934 Frieß, U., Klein Baltink, H., Beirle, S., Clèmer, K., Hendrick, F., Henzing, B., Irie, H., Leeuw, G. de, Li, A., Moerman,
935 M. M., Roozendaal, M. van, Shaiganfar, R., Wagner, T., Wang, Y., Xie, P., Yilmaz, S. and Zieger, P.: Intercomparison
936 of aerosol extinction profiles retrieved from MAX-DOAS measurements, *Atmos. Meas. Tech.*, 9, 3205–3222,
937 <https://doi.org/10.5194/amt-9-3205-2016>, 2016.

938 Frieß, U., Beirle, S., Alvarado Bonilla, L., Bösch, T., Friedrich, M. M., Hendrick, F., PETERS, A., Richter, A., van
939 Roozendaal, M., Rozanov, V. V., Spinei, E., TIRPITZ, J.-L., Vlemmix, T., Wagner, T., and Wang, Y.: Intercomparison
940 of MAX-DOAS vertical profile retrieval algorithms: studies using synthetic data, *Atmos. Meas. Tech.*, 12, 2155–2181,
941 <https://doi.org/10.5194/amt-12-2155-2019>, 2019.

942 Georgoulias, A. K., Boersma, K. F., van Vliet, J., Zhang, X., van der A, R., Zanis, P. and de Laat, J.: Detection of NO
943 2 pollution plumes from individual ships with the TROPOMI/S5P satellite sensor, *Environ. Res. Lett.*, 15(12), 124037,
944 [doi:10.1088/1748-9326/abc445](https://doi.org/10.1088/1748-9326/abc445), 2020.

945 Gielen, C., Hendrick, F., Pinardi, G., De Smedt, I., Fayt, C., Hermans, C., Stavrou, T., Bauwens, M., Müller, J.,
946 Ndenzako, E., Nzohabonayo, P., Akimana, R., Niyonzima, S., Van Roozendaal, M. and De Mazière, M.:
947 Characterisation of Central-African aerosol and trace-gas emissions based on MAX-DOAS measurements and model
948 simulations over, *Atmos. Chem. Phys. Discuss.*, (2), 1–41, [doi:10.5194/acp-2016-1104](https://doi.org/10.5194/acp-2016-1104), 2017.

949 González Abad, G., Liu, X., Chance, K., Wang, H., Kurosu, T. P. and Suleiman, R.: Updated Smithsonian
950 Astrophysical Observatory Ozone Monitoring Instrument (SAO OMI) formaldehyde retrieval, *Atmos. Meas. Tech.*,
951 8(1), 19–32, doi:10.5194/amt-8-19-2015, 2015.

952 González Abad, G., Vasilkov, A., Sefstor, C., Liu, X., and Chance, K.: Smithsonian Astrophysical Observatory Ozone
953 Mapping and Profiler Suite (SAO OMPS) formaldehyde retrieval, *Atmos. Meas. Tech.*, 9, 2797–2812,
954 <https://doi.org/10.5194/amt-9-2797-2016>, 2016.

955 Gonzalez Abad, G., Souri, A. H., Bak, J., Chance, K., Flynn, L. E., Krotkov, N. A., Lamsal, L., Li, C., Liu, X., Miller,
956 C. C., Nowlan, C. R., Suleiman, R. and Wang, H.: Five decades observing Earth's atmospheric trace gases using
957 ultraviolet and visible backscatter solar radiation from space, *J. Quant. Spectrosc. Radiat. Transf.*, 238, 106478,
958 doi:<https://doi.org/10.1016/j.jqsrt.2019.04.030>, 2019.

959 Hassinen, S., Balis, D., Bauer, H., Begoin, M., Delcloo, A., Eleftheratos, K., Gimeno Garcia, S., Granville, J., Grossi,
960 M., Hao, N., Hedelt, P., Hendrick, F., Hess, M., Heue, K.-P., Hovila, J., Jønh-Sørensen, H., Kalakoski, N., Kauppi,
961 A., Kiemle, S., Kins, L., Koukouli, M. E., Kujanpää, J., Lambert, J.-C., Lang, R., Lerot, C., Loyola, D., Pedernana,
962 M., Pinardi, G., Romahn, F., Van Roozendaal, M., Lutz, R., De Smedt, I., Stammes, P., Steinbrecht, W., Tamminen,
963 J., Theys, N., Tilstra, L. G., Tuinder, O. N. E., Valks, P., Zerefos, C., Zimmer, W. and Zyrichidou, I.: Overview of the
964 O3M SAF GOME-2 operational atmospheric composition and UV radiation data products and data availability,
965 *Atmos. Meas. Tech.*, 9(2), 383–407, doi:10.5194/amt-9-383-2016, 2016.

966 Heckel, A., Richter, A., Tarsu, T., Wittrock, F., Hak, C., Pundt, I., Junkermann, W., and Burrows, J. P.: MAX-DOAS
967 measurements of formaldehyde in the Po-Valley, *Atmos. Chem. Phys.*, 5, 909–918, [http://www.atmos-chem-](http://www.atmos-chem-phys.net/5/909/2005)
968 [phys.net/5/909/2005](http://www.atmos-chem-phys.net/5/909/2005), 2005.

969 Hewson, W., Bösch, H., Barkley, M. P. and De Smedt, I.: Characterisation of GOME-2 formaldehyde retrieval
970 sensitivity, *Atmospheric Measurement Techniques*, 6(2), 371–386, doi:10.5194/amt-6-371-2013, 2013.

971 Hendrick, F., Müller, J.-F., Clémer, K., Wang, P., De Mazière, M., Fayt, C., Gielen, C., Hermans, C., Ma, J. Z.,
972 Pinardi, G., Stavrou, T., Vlemmix, T. and Van Roozendaal, M.: Four years of ground-based MAX-DOAS
973 observations of HONO and NO₂ in the Beijing area, *Atmos. Chem. Phys.*, 14(2), 765–781, doi:10.5194/acp-14-765-
974 2014, 2014.

975 Honninger, G., von Friedeburg, C. and Platt, U.: Multi axis differential optical absorption spectroscopy (MAX-
976 DOAS), *Atmos. Chem. Phys.*, 4, 231–254, www.atmos-chem-phys.org/acp/4/231/, 2004.

977 Hoque, H. M. S., Irie, H., & Damiani, A. : First MAX-DOAS observations of formaldehyde and glyoxal in Phimai,
978 Thailand, *Journal of Geophysical Research: Atmospheres*, 123, 9957–9975, <https://doi.org/10.1029/2018JD028480>,
979 2018.

980 Irie, H., Kanaya, Y., Akimoto, H., Iwabuchi, H., Shimizu, a. and Aoki, K.: Dual-wavelength aerosol vertical profile
981 measurements by MAX-DOAS at Tsukuba , Japan, *Atmos. Chem. Phys.*, 9(2), 2741–2749, doi:10.5194/acp-8-341-
982 2008, 2009.

983 Irie, H., Takashima, H., Kanaya, Y., Boersma, K. F., Gast, L., Wittrock, F., Brunner, D., Zhou, Y. and Van
984 Roozendaal, M.: Eight-component retrievals from ground-based MAX-DOAS observations, *Atmos. Meas. Tech.*,
985 4(1), 1027–1044, doi:10.5194/amt-4-639-2011, 2011.

986 Irie, H., Boersma, K. F., Kanaya, Y., Takashima, H., Pan, X., and Wang, Z. F.: Quantitative bias estimates for
987 tropospheric NO₂ columns retrieved from SCIAMACHY, OMI, and GOME-2 using a common standard for East
988 Asia, *Atmos. Meas. Tech.*, 5, 2403-2411, doi:10.5194/amt-5-2403-2012, 2012.

989 Irie, H., T. Nakayama, A. Shimizu, A. Yamazaki, T. Nagai, A. Uchiyama, Y. Zaizen, S. Kagamitani, and Y. Matsumi,
990 Evaluation of MAX-DOAS aerosol retrievals by coincident observations using CRDS, lidar, and sky radiometer in
991 Tsukuba, Japan, *Atmospheric Measurement Techniques*, 8, 2775-2788, doi:10.5194/amt-8-2775-2015, 2015.

992 Irie, H., Hoque, H. M. S., Damiani, A., Okamoto, H., Fatmi, A. M., Khatri, P., Takamura, T., and Jarupongsakul, T.:
993 Simultaneous observations by sky radiometer and MAX-DOAS for characterization of biomass burning plumes in
994 central Thailand in January–April 2016, *Atmos. Meas. Tech.*, 12, 599–606, <https://doi.org/10.5194/amt-12-599-2019>,
995 2019.

996 Jin, X., Fiore, A. M. A. M. A. M., Murray, L. T. L. T., Valin, L. C. L. C., Lamsal, L. N. L. N. L. N., Duncan, B.,
997 Folkert Boersma, K., De Smedt, I., Abad, G. G. G. G., Chance, K., others and Tonnesen, G. S. G. S.: Evaluating a
998 space-based indicator of surface ozone-NO_x-VOC sensitivity over mid-latitude source regions and application to
999 decadal trends, *J. Geophys. Res. Atmos.*, 122(19), 439–461, doi:10.1002/2017JD026720, 2017.

1000 Jin, X., Fiore, A., Boersma, K. F., De Smedt, I. & Valin, L. Inferring changes in summertime surface ozone–NO_x–
1001 VOC chemistry over U.S. urban areas from two decades of satellite and ground-based observations. *Environ. Sci.*
1002 *Technol.* 54, 6518–6529, 2020.

1003 Jung, Y, González Abad, G., Nowlan, C. R., Chance, K., Liu, X., Torres, O., & Ahn, C.: Explicit aerosol correction
1004 of OMI formaldehyde retrievals. *Earth and Space Science*, 6, 2087-2105, <https://doi.org/10.1029/2019EA000702>,
1005 2019.

1006 Kaiser, J., Jacob, D. J., Zhu, L., Travis, K. R., Fisher, J. A., González Abad, G., Zhang, L., Zhang, X., Fried, A.,
1007 Crounse, J. D., St. Clair, J. M., and Wisthaler, A.: High-resolution inversion of OMI formaldehyde columns to quantify
1008 isoprene emission on ecosystem-relevant scales: application to the southeast US, *Atmos. Chem. Phys.*, 18, 5483–5497,
1009 <https://doi.org/10.5194/acp-18-5483-2018>, 2018.

1010 Khan, W. A., Khokhar, M. F., Shoaib, A. and Nawaz, R.: Monitoring and analysis of formaldehyde columns over
1011 Rawalpindi-Islamabad, Pakistan using MAX-DOAS and satellite observation, *Atmos. Pollut. Res.*, (November 2017),
1012 0–1, doi:10.1016/j.apr.2017.12.008, 2018.

1013 Kleipool, Q. L., Dobber, M. R., de Haan, J. F., and Levelt, P. F.: Earth surface reflectance climatology from 3 years
1014 of OMI data, *J. Geophys. Res.*, 113, D18308, <https://doi.org/10.1029/2008JD010290>, 2008.

1015 Kleipool, Q., Ludewig, A., Babić, L., Bartstra, R., Braak, R., Dierssen, W., Dewitte, P.-J., Kenter, P., Landzaat, R.,
1016 Leloux, J., Loots, E., Meijering, P., van der Plas, E., Rozemeijer, N., Schepers, D., Schiavini, D., Smeets, J., Vacanti,

1017 G., Vonk, F., and Veefkind, P.: Pre-launch calibration results of the TROPOMI payload on-board the Sentinel-5
1018 Precursor satellite, *Atmos. Meas. Tech.*, 11, 6439–6479, <https://doi.org/10.5194/amt-11-6439-2018>, 2018.

1019 Kreher, K., Van Roozendaal, M., Hendrick, F., Apituley, A., Dimitropoulou, E., Frieß, U., Richter, A., Wagner, T.,
1020 Lampel, J., Abuhassan, N., Ang, L., Anguas, M., Bais, A., Benavent, N., Bösch, T., Bogner, K., Borovski, A.,
1021 Bruchkouski, I., Cede, A., Chan, K. L., Donner, S., Drosoglou, T., Fayt, C., Finkenzeller, H., Garcia-Nieto, D., Gielen,
1022 C., Gómez-Martín, L., Hao, N., Henzing, B., Herman, J. R., Hermans, C., Hoque, S., Irie, H., Jin, J., Johnston, P.,
1023 Khayyam Butt, J., Khokhar, F., Koenig, T. K., Kuhn, J., Kumar, V., Liu, C., Ma, J., Merlaud, A., Mishra, A. K.,
1024 Müller, M., Navarro-Comas, M., Ostendorf, M., Pazmino, A., Peters, E., Pinardi, G., Pinharanda, M., PETERS, A., Platt,
1025 U., Postlyakov, O., Prados-Roman, C., Puertedura, O., Querel, R., Saiz-Lopez, A., Schönhardt, A., Schreier, S. F.,
1026 Seyler, A., Sinha, V., Spinei, E., Strong, K., Tack, F., Tian, X., Tiefengraber, M., Tirpitz, J.-L., van Gent, J., Volkamer,
1027 R., Vrekoussis, M., Wang, S., Wang, Z., Wenig, M., Wittrock, F., Xie, P. H., Xu, J., Yela, M., Zhang, C., and Zhao,
1028 X.: Intercomparison of NO₂, O₄, O₃ and HCHO slant column measurements by MAX-DOAS and zenith-sky UV–
1029 visible spectrometers during CINDI-2, *Atmos. Meas. Tech.*, 13, 2169–2208, [https://doi.org/10.5194/amt-13-2169-](https://doi.org/10.5194/amt-13-2169-2020)
1030 2020, 2020.

1031 Kumar, V., Beirle, S., Dörner, S., Mishra, A. K., Donner, S., Wang, Y., Sinha, V., and Wagner, T.: Long-term MAX-
1032 DOAS measurements of NO₂, HCHO, and aerosols and evaluation of corresponding satellite data products over
1033 Mohali in the Indo-Gangetic Plain, *Atmos. Chem. Phys.*, 20, 14183–14235, [https://doi.org/10.5194/acp-20-14183-](https://doi.org/10.5194/acp-20-14183-2020)
1034 2020, 2020.

1035 Kwon, H.-A., Park, R. J., González Abad, G., Chance, K., Kurosu, T. P., Kim, J., Smedt, I. De, Roozendaal, M. Van,
1036 Peters, E. and Burrows, J.: Description of a formaldehyde retrieval algorithm for the Geostationary Environment
1037 Monitoring Spectrometer (GEMS), *Atmos. Meas. Tech.*, 12(7), 3551–3571, 2019.

1038 Langen, J., Meijer, Y., Brinksma, E., Veißelmann, B., and Ingmann, P.: Copernicus Sentinels 4 and 5 Mission
1039 Requirements Traceability Document (MRTD), ESA, EOP-SM/2413/BV-bv , issue: 2, 2017.

1040 Levelt, P. F., van den Oord, G. H. ., Dobber, M. R., Malkki, A., Visser, H., de Vries, J., Stammes, P., Lundell, J. O. .
1041 and Saari, H.: The ozone monitoring instrument, *IEEE Trans. on Geosc. and Rem. Sens.*, 44(5), 1093–1101, 2006.

1042 Levelt, P. F., Joiner, J., Tamminen, J., Veefkind, J. P., Bhartia, P. K., Fioletov, V., Carn, S., Laatz, J. De, Deland, M.,
1043 Marchenko, S. and Mcpeters, R.: The Ozone Monitoring Instrument : overview of 14 years in space, *Atmos. Chem.*
1044 *Phys.*, (18), 5699–5745, 2018.

1045 Levelt, P.F., Stein Zweers, Aben, Bauwens, Borsdorff, De Smedt, J. Eskes, Lerot, Loyola, Romahn, Stavrou, Theys,
1046 Van Roozendaal, Veefkind, Verhoels: Air Quality Impacts of COVID-19 Lockdown Measures detected from space
1047 using high spatial resolution observations of multiple trace gases from Sentinel-5P/TROPOMI, to be submitted to
1048 ACP, 2021.

1049 Li, X., Brauers, T., Shao, M., Garland, R. M., Wagner, T., Deutschmann, T. and Wahner, A.: MAX-DOAS
1050 measurements in southern China: retrieval of aerosol extinctions and validation using ground-based in-situ data,
1051 *Atmos. Chem. Phys.*, 10(5), 2079–2089, doi:10.5194/acp-10-2079-2010, 2010.

1052 Li, C., Joiner, J., Krotkov, N. A., and Dunlap, L.: A new method for global retrievals of HCHO total columns from
1053 the Suomi National Polar-orbiting Partnership Ozone Mapping and Profiler Suite. *Geophys. Res. Lett.*, 42, 2515–
1054 2522. doi: 10.1002/2015GL063204, 2015.

1055 Li, K., Jacob, D. J., Shen, L., Lu, X., De Smedt, I., and Liao, H.: Increases in surface ozone pollution in China from
1056 2013 to 2019: anthropogenic and meteorological influences, *Atmos. Chem. Phys.*, 20, 11423–11433,
1057 <https://doi.org/10.5194/acp-20-11423-2020>, 2020.

1058 ~~Lorente, A., Folkert Boersma, K., Yu, H., Dörner, S., Hilboll, A., Richter, A., Liu, M., Lamsal, L. N., Barkley, M.,~~
1059 ~~De Smedt, I., Van Roozendael, M., Wang, Y., Wagner, T., Beirle, S., Lin, J.-T., Krotkov, N., Stammes, P., Wang, P.,~~
1060 ~~Eskes, H. J., and Krol, M.: Structural uncertainty in air mass factor calculation for NO₂ and HCHO satellite retrievals,~~
1061 ~~*Atmos. Meas. Tech.*, 10, 759–782, <https://doi.org/10.5194/amt-10-759-2017>, 2017.~~

1062 ~~Lorente, A., Folkert Boersma, K., Yu, H., Dörner, S., Hilboll, A., Richter, A., Liu, M., Lamsal, L. N., Barkley, M.,~~
1063 ~~De Smedt, I., Van Roozendael, M., Wang, Y., Wagner, T., Beirle, S., Lin, J. T., Krotkov, N., Stammes, P., Wang, P.,~~
1064

1065 Loyola, D. G., Xu, J., Heue, K.-P., and Zimmer, W.: Applying FP_ILM to the retrieval of geometry-dependent
1066 effective Lambertian equivalent reflectivity (GE_LER) daily maps from UVN satellite measurements, *Atmos. Meas.*
1067 *Tech.*, 13, 985–999, <https://doi.org/10.5194/amt-13-985-2020>, 2020.

1068 Eskes, H. J., and Krol, M.: Structural uncertainty in air mass factor calculation for NO₂ and HCHO satellite retrievals,
1069 *Atmos. Meas. Tech.*, 10, 759–782, <https://doi.org/10.5194/amt-10-759-2017>, 2017.

1070 Loyola, D. G., Gimeno García, S., Lutz, R., Argyrouli, A., Romahn, F., Spurr, R. J. D., Pedernana, M., Doicu, A.,
1071 Molina García, V., and Schüssler, O.: The operational cloud retrieval algorithms from TROPOMI on board Sentinel-
1072 5 Precursor, *Atmos. Meas. Tech.*, 11, 409–427, <https://doi.org/10.5194/amt-11-409-2018>, 2018.

1073 Ludwig, A., Kleipool, Q., Bartstra, R., Landzaat, R., Leloux, J., Loots, E., Meijering, P., van der Plas, E., Rozemeijer,
1074 N., Vonk, F., and Veeffkind, P.: In-flight calibration results of the TROPOMI payload on board the Sentinel-5
1075 Precursor satellite, *Atmos. Meas. Tech.*, 13, 3561–3580, <https://doi.org/10.5194/amt-13-3561-2020>, 2020.

1076 Ma, J. Z., Beirle, S., Jin, J. L., Shaiganfar, R., Yan, P., and Wagner, T.: Tropospheric NO₂ vertical column densities
1077 over Beijing: results of the first three years of ground-based MAX-DOAS measurements (2008–2011) and satellite
1078 validation, *Atmos. Chem. Phys.*, 13, 1547–1567, doi:10.5194/acp-13-1547-2013, 2013.

1079 Mahajan, A. S., De Smedt, I., Biswas, M. S., Ghude, S., Fadnavis, S., Roy, C. and van Roozendael, M.: Inter-annual
1080 variations in satellite observations of nitrogen dioxide and formaldehyde over India, *Atmos. Environ.*, 116, 194–201,
1081 doi:10.1016/j.atmosenv.2015.06.004, 2015.

1082 ~~Marais, E. A., Jacob, D. J., Kurosu, T. P., Chance, K., Murphy, J. G., Reeves, C., Mills, G., Casadio, S., Millet, D. B.,~~
1083 ~~Barkley, M. P., Paulot, F., and Mao, J.: Isoprene emissions in Africa inferred from OMI observations of formaldehyde~~
1084 ~~columns, *Atmos. Chem. Phys.*, 12, 6219–6235, <https://doi.org/10.5194/acp-12-6219-2012>, 2012. Marais, E. A., Jacob,~~
1085 ~~D. J., Kurosu, T. P., Chance, K., Murphy, J. G., Reeves, C., Mills, G., Casadio, S., Millet, D. B., Barkley, M. P.,~~

1086 [Paulot, F., et al.: Isoprene emissions in Africa inferred from OMI observations of formaldehyde columns, Atmos.](#)
1087 [Chem. Phys. Discuss., 12\(3\), 7475–7520, doi:10.5194/acpd-12-7475-2012, 2012.](#)

1088 Marbach, T., Beirle, S., Platt, U., Hoor, P., Wittrock, F., Richter, A., Vrekoussis, M., Grzegorski, M., Burrows, J. P.
1089 and Wagner, T.: Satellite measurements of formaldehyde linked to shipping emissions, *Atmos. Chem. Phys.*, 9(21),
1090 8223–8234, doi:10.5194/acp-9-8223-2009, 2009.

1091 Meller, R. and Moortgat, G. K.: Temperature dependence of the absorption cross section of HCHO between 223 and
1092 323 K in the wavelength range 225–375 nm, *J. Geophys. Res.*, 105, 7089–7102,
1093 <https://doi.org/10.1029/1999JD901074>, 2000.

1094 Millet, D. B., Jacob, D. J., Boersma, K. F., Fu, T.-M., Kurosu, T. P., Chance, K. V., Heald, C. L. and Guenther, A.:
1095 Spatial distribution of isoprene emissions from North America derived from formaldehyde column measurements by
1096 the OMI satellite sensor, *Journal of Geophysical Research*, 113(D2), 1-18, doi:10.1029/2007JD008950, 2008.

1097 Nightingale, J., Boersma, K., Muller, J.-P., Compornolle, S., Lambert, J.-C., Blessing, S., Giering, R., Gobron, N., De
1098 Smedt, I., Coheur, P. and others: Quality assurance framework development based on six new ECV data products to
1099 enhance user confidence for climate applications, *Remote Sens.*, 10(8), 1254, 2018.

1100 [Opacka, B., Müller, J.-F., Stavrakou, T., Bauwens, M., Sindelarova, K., Markova, J., and Guenther, A. B.: Global and](#)
1101 [regional impacts of land cover changes on isoprene emissions derived from spaceborne data and the MEGAN model,](#)
1102 [Atmos. Chem. Phys., 21, 8413–8436, https://doi.org/10.5194/acp-21-8413-2021, 2021](#) ~~Opacka, B., Müller, J.-F.,~~
1103 ~~Stavrakou, T., Bauwens, M., Sindelarova, K., Markova, J., and Guenther, A. B.: Global and regional impacts of land~~
1104 ~~cover changes on isoprene emissions derived from spaceborne data and the MEGAN model, Atmos. Chem. Phys-~~
1105 ~~Discuss. [preprint], https://doi.org/10.5194/acp-2021-95, in review, 2021.~~

1106 Palmer, P. I., Jacob, D. J., Chance, K. V., Martin, R. V., D, R. J., Kurosu, T. P., Bey, I., Yantosca, R. and Fiore, A.:
1107 Air mass factor formulation for spectroscopic measurements from satellites: Application to formaldehyde retrievals
1108 from the Global Ozone Monitoring Experiment, *Journal of Geophysical Research*, 106(D13), 14539-14550,
1109 doi:10.1029/2000JD900772, 2001.

1110 Pinardi, G., Van Roozendael, M., Abuhassan, N., Adams, C., Cede, A., Clémer, K., Fayt, C., Frieß, U., Gil, M.,
1111 Herman, J., Hermans, C., Hendrick, F., Irie, H., Merlaud, A., Navarro Comas, M., Peters, E., Piters, A. J. M.,
1112 Puentedura, O., Richter, A., Schönhardt, A., Shaiganfar, R., Spinei, E., Strong, K., Takashima, H., Vrekoussis, M.,
1113 Wagner, T., Wittrock, F., and Yilmaz, S.: MAX-DOAS formaldehyde slant column measurements during CINDI:
1114 inter-comparison and analysis improvement, *Atmos. Meas. Tech.*, 6, 167-185, doi:10.5194/amt-6-167-2013, 2013.

1115 Platt, U and Stutz, J.: *Differential Optical Absorption Spectroscopy: Principles and Applications (Physics of Earth and*
1116 *Space Environments)*, Springer-Verlag, Berlin, Heidelberg, ISBN 978-3540211938, 2008.

1117 Richter, A., Eyring, V., Burrows, J. P., Bovensmann, H., Lauer, A., Sierk, B., and Crutzen, P. J., Satellite
1118 measurements of NO₂ from international shipping emissions, *Geophys. Res. Lett.*, 31, L23110,
1119 doi:10.1029/2004GL020822, 2004.

1120 Richter, A., Begoin, M., Hilboll, A. and Burrows, J.P.: An improved NO₂ retrieval for the GOME-2 satellite
1121 instrument, *Atmos. Meas. Tech.*, 4(1), 1147–1159, doi:10.5194/amt-4-213-2011, 2011.

1122 Richter, A., Hilboll, A., Sanders, A., Peters, E. and Burrows, J.P.: Inhomogeneous scene effects in OMI NO₂
1123 observations, *Geophysical Research Abstracts*, EGU General Assembly 2018, Vol. 20, EGU2018-9630-3,
1124 <https://meetingorganizer.copernicus.org/EGU2018/EGU2018-9630-3.pdf>, 2018. Richter, A., Hilboll, A., Sanders, A.
1125 and Burrows, J.P.: Inhomogeneous scene effects in TROPOMI satellite data, 9th DOAS Workshop, 13-15 July 2020,
1126 Utrecht, 2020.

1127 Rivera Cárdenas, C., Guarín, C., Stremme, W., Friedrich, M. M., Bezanilla, A., Rivera Ramos, D., Mendoza-
1128 Rodríguez, C. A., Grutter, M., Blumenstock, T., and Hase, F.: Formaldehyde total column densities over Mexico City:
1129 comparison between multi-axis differential optical absorption spectroscopy and solar-absorption Fourier transform
1130 infrared measurements, *Atmos. Meas. Tech.*, 14, 595–613, <https://doi.org/10.5194/amt-14-595-2021>, 2021.

1131 Rodgers, C. D.: *Inverse Methods for Atmospheric Sounding, Theory and Practice*, World Scientific Publishing,
1132 Singapore-New-Jersey-London-Hong Kong, 2000.

1133 Rodgers, C. D., and B. J. Connor: Intercomparison of remote sounding instruments, *J. Geophys. Res.*, 108,
1134 doi:10.1029/2002JD002299, 2003.

1135

1136 ~~[Ryan, R. G., Silver, J. D., Querel, R., Smale, D., Rhodes, S., Tully, M., Jones, N., and Schofield, R.: Comparison of](#)~~
1137 ~~[formaldehyde tropospheric columns in Australia and New Zealand using MAX-DOAS, FTIR and TROPOMI, *Atmos.*](#)~~
1138 ~~[Meas. Tech.](#), 13, 6501–6519, <https://doi.org/10.5194/amt-13-6501-2020>, 2020~~~~[Ryan, R. G., Silver, J. D., Querel, R.,](#)~~
1139 ~~[Smale, D., Rhodes, S., Tully, M., Jones, N., and Schofield, R.: Comparison of formaldehyde tropospheric columns in](#)~~
1140 ~~[Australia and New Zealand using MAX-DOAS, FTIR and TROPOMI, *Atmos. Meas. Tech. Discuss.*](#)~~
1141 ~~[https://doi.org/10.5194/amt-2020-232](#), in review, 2020.~~

1142 Sen, P. K.: Estimates of the regression coefficient based on Kendall's tau, *J. Am. Stat. Assoc.*, 63, 1379–1389,
1143 <https://doi.org/10.2307/2285891>, 1968.

1144 Shen, L., Jacob, D. J., Zhu, L., Zhang, Q., Zheng, B., Sulprizio, M. P., Li, K., De Smedt, I., González Abad, G., Cao,
1145 H. and others: The 2005–2016 trends of formaldehyde columns over China observed by satellites: Increasing
1146 anthropogenic emissions of volatile organic compounds and decreasing agricultural fire emissions, *Geophys. Res.*
1147 *Let.*, 46(8), 4468–4475, 2019.

1148 Sinreich, R., Frieß, U., Wagner, T., and Platt, U.: Multi axis differential optical absorption spectroscopy (MAX-
1149 DOAS) of gas and aerosol distributions, *Faraday Discuss.*, 130, 153–164, <https://doi.org/10.1039/B419274P>, 2005.

1150 Song, C. H., Kim, H. S., von Glasow, R., Brimblecombe, P., Kim, J., Park, R. J., Woo, J. H., and Kim, Y. H.: Source
1151 identification and budget analysis on elevated levels of formaldehyde within the ship plumes: a ship-plume
1152 photochemical/dynamic model analysis, *Atmos. Chem. Phys.*, 10, 11969–11985, [https://doi.org/10.5194/acp-10-](https://doi.org/10.5194/acp-10-11969-2010)
1153 11969-2010, 2010

Formatted: Don't keep lines together

1154 Souri, A. H., Nowlan, C. R., Wolfe, G. M., Lamsal, L. N., Chan Miller, C. E., Abad, G. G., Janz, S. J., Fried, A.,
1155 Blake, D. R., Weinheimer, A. J., Diskin, G. S., Liu, X. and Chance, K.: Revisiting the effectiveness of HCHO/NO₂
1156 ratios for inferring ozone sensitivity to its precursors using high resolution airborne remote sensing observations in a
1157 high ozone episode during the KORUS-AQ campaign, *Atmos. Environ.*, 224, 117341,
1158 doi:<https://doi.org/10.1016/j.atmosenv.2020.117341>, 2020.

1159 Spurr, R. J. D.: LIDORT and VLIDORT: Linearized pseudo-spherical scalar and vector discrete ordinate radiative
1160 transfer models for use in remote sensing retrieval problems, in *Light Scattering Reviews*, edited by: Kokhanovsky,
1161 A., 229–271, Berlin, 2008.

1162 Stavrakou, T., Müller, J.-F., Bauwens, M., De Smedt, I., Van Roozendael, M., Guenther, A., Wild, M. and Xia, X.:
1163 Isoprene emissions over Asia 1979–2012: impact of climate and land-use changes, *Atmos. Chem. Phys.*, 14(9), 4587–
1164 4605, 2014.

1165 Stavrakou, T., Müller, J.-F., Bauwens, M., De Smedt, I., Van Roozendael, M., De Mazière, M., Vigouroux, C.,
1166 Hendrick, F., George, M., Clerbaux, C., Coheur, P.-F., and Guenther, A.: How consistent are top-down hydrocarbon
1167 emissions based on formaldehyde observations from GOME-2 and OMI?, *Atmos. Chem. Phys.*, 15, 11861–11884,
1168 <https://doi.org/10.5194/acp-15-11861-2015>, 2015.

1169 Stavrakou, T., Müller, J.-F., Bauwens, M., De Smedt, I., Lerot, C., Van Roozendael, M., Coheur, P.-F., Clerbaux, C.,
1170 Boersma, K. F., van der A, R. and Song, Y.: Substantial Underestimation of Post-Harvest Burning Emissions in the
1171 North China Plain Revealed by Multi-Species Space Observations, *Sci. Rep.*, 6(1), 32307, doi:10.1038/srep32307,
1172 2016.

1173 Stavrakou, T., Müller, J.-F., Bauwens, M., De Smedt, I., Van Roozendael, M. and Guenther, A.: Impact of Short-Term
1174 Climate Variability on Volatile Organic Compounds Emissions Assessed Using OMI Satellite Formaldehyde
1175 Observations, *Geophys. Res. Lett.*, 45(16), 8681–8689, 2018.

1176 Su, W., Liu, C., Hu, Q., Zhao, S., Sun, Y., Wang, W., Zhu, Y., Liu, J., and Kim, J.: Primary and secondary sources of
1177 ambient formaldehyde in the Yangtze River Delta based on Ozone Mapping and Profiler Suite (OMPS) observations,
1178 *Atmos. Chem. Phys.*, 19, 6717–6736, <https://doi.org/10.5194/acp-19-6717-2019>, 2019.

1179 Su, W., Liu, C., Chan, K. L., Hu, Q., Liu, H., Ji, X., Zhu, Y., Liu, T., Zhang, C., Chen, Y., and Liu, J.: An improved
1180 TROPOMI tropospheric HCHO retrieval over China, *Atmos. Meas. Tech.*, 13, 6271–6292,
1181 <https://doi.org/10.5194/amt-13-6271-2020>, 2020.

1182 Sun, W., Zhu, L., De Smedt, I., Bai, B., Pu, D., Chen, Y., et al.: Global significant changes in formaldehyde (HCHO)
1183 columns observed from space at the early stage of the COVID-19 pandemic. *Geophysical Research Letters*, 48,
1184 e2020GL091265. <https://doi.org/10.1029/2020GL091265>, 2021.

1185 Surl, L., Palmer, P. I., and González Abad, G.: Which processes drive observed variations of HCHO columns over
1186 India?, *Atmos. Chem. Phys.*, 18, 4549–4566, <https://doi.org/10.5194/acp-18-4549-2018>, 2018.

1187 Theys, N., De Smedt, I., van Gent, J., Danckaert, T., Wang, T., Hendrick, F., Stavrakou, T., Bauduin, S., Clarisse, L.,
1188 Li, C., Krotkov, N., Yu, H., Brenot, H. and Van Roozendael, M.: Sulfur dioxide vertical column DOAS retrievals
1189 from the Ozone Monitoring Instrument: Global observations and comparison to ground-based and satellite data, *J.*
1190 *Geophys. Res. Atmos.*, 120(6), 2014JD022657, doi:10.1002/2014JD022657, 2015.

1191 Theys, N., Volkamer, R., Müller, J. F., Zarzana, K. J., Kille, N., Clarisse, L., De Smedt, I., Lerot, C., Finkenzeller, H.,
1192 Hendrick, F., Koenig, T. K., Lee, C. F., Knote, C., Yu, H. and Van Roozendael, M.: Global nitrous acid emissions and
1193 levels of regional oxidants enhanced by wildfires, *Nat. Geosci.*, 13(10), 681–686, doi:10.1038/s41561-020-0637-7,
1194 2020.

1195 Tirpitz, J.-L., Frieß, U., Hendrick, F., Alberti, C., Allaart, M., Apituley, A., Bais, A., Beirle, S., Berkhout, S., Bogner,
1196 K., Bösch, T., Bruchkouski, I., Cede, A., Chan, K. L., den Hoed, M., Donner, S., Drosoglou, T., Fayt, C., Friedrich,
1197 M. M., Frumau, A., Gast, L., Gielen, C., Gomez-Martín, L., Hao, N., Hensen, A., Henzing, B., Hermans, C., Jin, J.,
1198 Kreher, K., Kuhn, J., Lampel, J., Li, A., Liu, C., Liu, H., Ma, J., Merlaud, A., Peters, E., Pinardi, G., PETERS, A., Platt,
1199 U., Puentedura, O., Richter, A., Schmitt, S., Spinei, E., Stein Zweers, D., Strong, K., Swart, D., Tack, F., Tiefengraber,
1200 M., van der Hoff, R., van Roozendael, M., Vlemmix, T., Vonk, J., Wagner, T., Wang, Y., Wang, Z., Wenig, M.,
1201 Wiegner, M., Wittrock, F., Xie, P., Xing, C., Xu, J., Yela, M., Zhang, C., and Zhao, X.: Intercomparison of MAX-
1202 DOAS vertical profile retrieval algorithms: studies on field data from the CINDI-2 campaign, *Atmos. Meas. Tech.*,
1203 14, 1–35, <https://doi.org/10.5194/amt-14-1-2021>, 2021.

1204 van Geffen, J., Boersma, K. F., Eskes, H., Sneep, M., ter Linden, M., Zara, M., and Veefkind, J. P.: S5P TROPOMI
1205 NO₂ slant column retrieval: method, stability, uncertainties and comparisons with OMI, *Atmos. Meas. Tech.*, 13,
1206 1315–1335, <https://doi.org/10.5194/amt-13-1315-2020>, 2020.

1207 Veefkind, J. P., Aben, I., McMullan, K., Förster, H., de Vries, J., Otter, G., Claas, J., Eskes, H. J., de Haan, J. F.,
1208 Kleipool, Q., van Weele, M., et al.: TROPOMI on the ESA Sentinel-5 Precursor: A GMES mission for global
1209 observations of the atmospheric composition for climate, air quality and ozone layer applications, *Remote Sensing of*
1210 *Environment*, 120(0), 70-83, 2012.

1211 Veefkind, J. P., de Haan, J. F., Sneep, M., and Levelt, P. F.: Improvements to the OMI O₂–O₂ operational cloud
1212 algorithm and comparisons with ground-based radar–lidar observations, *Atmos. Meas. Tech.*, 9, 6035-6049,
1213 <https://doi.org/10.5194/amt-9-6035-2016>, 2016.

1214 Verhoelst, T., Compernelle, S., Pinardi, G., Lambert, J.-C., Eskes, H. J., Eichmann, K.-U., Fjæraa, A. M., Granville,
1215 J., Niemeijer, S., Cede, A., Tiefengraber, M., Hendrick, F., Pazmiño, A., Bais, A., Bazureau, A., Boersma, K. F.,
1216 Bogner, K., Dehn, A., Donner, S., Elokhov, A., Gebetsberger, M., Goutail, F., Grutter de la Mora, M., Gruzdev, A.,
1217 Gratsea, M., Hansen, G. H., Irie, H., Jepsen, N., Kanaya, Y., Karagkiozidis, D., Kivi, R., Kreher, K., Levelt, P. F.,
1218 Liu, C., Müller, M., Navarro Comas, M., PETERS, A. J. M., Pommereau, J.-P., Portafaix, T., Prados-Roman, C.,
1219 Puentedura, O., Querel, R., Remmers, J., Richter, A., Rimmer, J., Rivera Cárdenas, C., Saavedra de Miguel, L.,
1220 Sinyakov, V. P., Stremme, W., Strong, K., Van Roozendael, M., Veefkind, J. P., Wagner, T., Wittrock, F., Yela
1221 González, M., and Zehner, C.: Ground-based validation of the Copernicus Sentinel-5P TROPOMI NO₂ measurements

1222 with the NDACC ZSL-DOAS, MAX-DOAS and Pandonia global networks, *Atmos. Meas. Tech.*, 14, 481–510,
1223 <https://doi.org/10.5194/amt-14-481-2021>, 2021.

1224 Vigouroux, C., Hendrick, F., Stavrakou, T., Dils, B., De Smedt, I., Hermans, C., Merlaud, A., Scolas, F., Senten, C.,
1225 Vanhaelewyn, G., Fally, S., Carleer, M., Metzger, J.-M., Müller, J.-F., Van Roozendael, M., and De Mazière, M.:
1226 Ground-based FTIR and MAX-DOAS observations of formaldehyde at Réunion Island and comparisons with satellite
1227 and model data, *Atmos. Chem. Phys.*, 9, 9523–9544, doi:10.5194/acp-9-9523-2009, 2009.

1228 Vigouroux, C., Bauer Aquino, C. A., Bauwens, M., Becker, C., Blumenstock, T., De Mazière, M., García, O., Grutter,
1229 M., Guarin, C., Hannigan, J., Hase, F., Jones, N., Kivi, R., Koshelev, D., Langerock, B., Lutsch, E., Makarova, M.,
1230 Metzger, J.-M., Müller, J.-F., Notholt, J., Ortega, I., Palm, M., Paton-Walsh, C., Poberovskii, A., Rettinger, M.,
1231 Robinson, J., Smale, D., Stavrakou, T., Stremme, W., Strong, K., Sussmann, R., Té, Y., and Toon, G.: NDACC
1232 harmonized formaldehyde time series from 21 FTIR stations covering a wide range of column abundances, *Atmos.*
1233 *Meas. Tech.*, 11, 5049–5073, <https://doi.org/10.5194/amt-11-5049-2018>, 2018.

1234 Vigouroux, C., Langerock, B., Bauer Aquino, C. A., Blumenstock, T., Cheng, Z., De Mazière, M., De Smedt, I.,
1235 Grutter, M., Hannigan, J. W., Jones, N., Kivi, R., Loyola, D., Lutsch, E., Mahieu, E., Makarova, M., Metzger, J.-M.,
1236 Morino, I., Murata, I., Nagahama, T., Notholt, J., Ortega, I., Palm, M., Pinaridi, G., Röhling, A., Smale, D., Stremme,
1237 W., Strong, K., Sussmann, R., Té, Y., van Roozendael, M., Wang, P., and Winkler, H.: TROPOMI–Sentinel-5
1238 Precursor formaldehyde validation using an extensive network of ground-based Fourier-transform infrared stations,
1239 *Atmos. Meas. Tech.*, 13, 3751–3767, <https://doi.org/10.5194/amt-13-3751-2020>, 2020.

1240 Vlemmix, T., PETERS, A., StAMMES, P., Wang, P. and Levelt, P. F.: Retrieval of tropospheric NO₂ using the MAX-
1241 DOAS method combined with relative intensity measurements for aerosol correction, *Atmos. Meas. Tech.*, 3(5),
1242 1287–1305, doi:10.5194/amt-3-1287-2010, 2010.

1243 Vlemmix, T., Hendrick, F., Pinaridi, G., Smedt, I. De, Fayt, C., Hermans, C., PETERS, A., Wang, P. and Levelt, P.: MAX-
1244 DOAS observations of aerosols, formaldehyde and nitrogen dioxide in the Beijing area: comparison of two profile
1245 retrieval, *Atmos. Meas. Tech.*, (2), 941–963, doi:10.5194/amt-8-941-2015, 2015.

1246 Vrekoussis, M., Wittrock, F., Richter, A. and Burrows, J. P.: GOME-2 observations of oxygenated VOCs: what can
1247 we learn from the ratio glyoxal to formaldehyde on a global scale?, *Atmos. Chem. Phys.*, 10(21), 10145–10160, 2010.

1248 Wagner, T., Dix, B., Friedeburg, C. Von, Friess, U., Sanghavi, S., Sinreich, R. and Platt, U.: MAX-DOAS O₄
1249 measurements: a new technique to derive information on atmospheric aerosols - Principles and information content,
1250 *J. Geophys. Res.*, 109(D22205), 2004.

1251 Wagner, T., Beirle, S., Brauers, T., Deutschmann, T., Frieß, U., Hak, C., Halla, J. D., Heue, K. P., Junkermann, W.,
1252 Li, X., Platt, U., and Pundt-Gruber, I.: Inversion of tropospheric profiles of aerosol extinction and HCHO and NO₂
1253 mixing ratios from MAX-DOAS observations in Milano during the summer of 2003 and comparison with independent
1254 data sets, *Atmos. Meas. Tech.*, 4, 2685–2715, doi:10.5194/amt-4-2685-2011, 2011.

1255 Wang, Y., Beirle, S., Hendrick, F., Hilboll, A., Jin, J., Kyuberis, A. A., Lampel, J., Li, A., Luo, Y., Lodi, L., Ma, J.,
1256 Navarro, M., Ortega, I., Peters, E., Polyansky, O. L., Remmers, J., Richter, A., Puentedura, O., Van Roozendaal, M.,
1257 Seyler, A., Tennyson, J., Volkamer, R., Xie, P., Zobov, N. F., and Wagner, T.: MAX-DOAS measurements of HONO
1258 slant column densities during the MAD-CAT campaign: inter-comparison, sensitivity studies on spectral analysis
1259 settings, and error budget, *Atmos. Meas. Tech.*, 10, 3719–3742, <https://doi.org/10.5194/amt-10-3719-2017>, 2017.

1260 Wang, Y., Dörner, S., Donner, S., Böhnke, S., Smedt, I. De, Dickerson, R. R., Dong, Z., He, H., Li, Z., Li, Z. and
1261 others: Vertical profiles of NO₂, SO₂, HONO, HCHO, CHOCHO and aerosols derived from MAX-DOAS
1262 measurements at a rural site in the central western North China Plain and their relation to emission sources and effects
1263 of regional transport, *Atmos. Chem. Phys.*, 19(8), 5417–5449, 2019a.

1264 Wang, Y., Wang, Z., Yu, C., Zhu, S., Cheng, L., Zhang, Y. and Chen, L.: Validation of OMI HCHO Products Using
1265 MAX-DOAS observations from 2010 to 2016 in Xianghe, Beijing: Investigation of the Effects of Aerosols on Satellite
1266 Products, *Remote Sens.*, 11(2), 203, doi:10.3390/rs11020203, 2019b.

1267 Wells, K. C., Millet, D. B., Payne, V. H., Deventer, M. J., Bates, K. H., Gouw, J. A., Graus, M., Warneke, C.,
1268 Wisthaler, A. and Fuentes, J. D.: Satellite isoprene retrievals constrain emissions and atmospheric oxidation, *Nature*,
1269 585(August 2019), doi:10.1038/s41586-020-2664-3, 2020.

1270 Williams, J. E., Boersma, K. F., Le Sager, P., and Verstraeten, W. W.: The high-resolution version of TM5-MP for
1271 optimized satellite retrievals: description and validation, *Geosci. Model Dev.*, 10, 721–750,
1272 <https://doi.org/10.5194/gmd-10-721-2017>, 2017.

1273 Wittrock, F., Oetjen, H., Richter, A., Fietkau, S., Medeke, T., Rozanov, A., and Burrows, J.P.: MAX-DOAS
1274 measurements of atmospheric trace gases in Ny-Alesund – Radiative transfer studies and their application, *Atmos.*
1275 *Chem. Phys.*, 4, 955–966, doi:10.5194/acp-4-955-2004, 2004.

1276 Wittrock, F., Richter, A., Oetjen, H., Burrows, J. P., Kanakidou, M., Myriokefalitakis, S., Volkamer, R., Beirle, S.,
1277 Platt, U. and Wagner, T.: Simultaneous global observations of glyoxal and formaldehyde from space, *Geophysical*
1278 *Research Letters*, 33(16), 1-5, doi:10.1029/2006GL026310, 2006.

1279 Zara, M., Boersma, K. F., De Smedt, I., Richter, A., Peters, E., van Geffen, J. H. G. M., Beirle, S., Wagner, T., Van
1280 Roozendaal, M., Marchenko, S., Lamsal, L. N., and Eskes, H. J.: Improved slant column density retrieval of nitrogen
1281 dioxide and formaldehyde for OMI and GOME-2A from QA4ECV: intercomparison, uncertainty characterisation,
1282 and trends, *Atmos. Meas. Tech.*, 11, 4033–4058, <https://doi.org/10.5194/amt-11-4033-2018>, 2018.

1283 Zhu, L., Jacob, D. J., Kim, P. S., Fisher, J. A., Yu, K., Travis, K. R., Mickley, L. J., Yantosca, R. M., Sulprizio, M. P.,
1284 De Smedt, I., González Abad, G., Chance, K., Li, C., Ferrare, R., Fried, A., Hair, J. W., Hanisco, T. F., Richter, D.,
1285 Jo Scarino, A., Walega, J., Weibring, P., and Wolfe, G. M.: Observing atmospheric formaldehyde (HCHO) from
1286 space: validation and intercomparison of six retrievals from four satellites (OMI, GOME2A, GOME2B, OMPS) with
1287 SEAC4RS aircraft observations over the southeast US, *Atmos. Chem. Phys.*, 16, 13477–13490,
1288 <https://doi.org/10.5194/acp-16-13477-2016>, 2016.

- 1289 Zhu, L., González Abad, G., Nowlan, C. R., Chan Miller, C., Chance, K., Apel, E. C., DiGangi, J. P., Fried, A.,
1290 Hanisco, T. F., Hombrook, R. S., Hu, L., Kaiser, J., Keutsch, F. N., Permar, W., St. Clair, J. M., and Wolfe, G. M.:
1291 Validation of satellite formaldehyde (HCHO) retrievals using observations from 12 aircraft campaigns, *Atmos. Chem.*
1292 *Phys.*, 20, 12329–12345, <https://doi.org/10.5194/acp-20-12329-2020>, 2020.
- 1293 Zyrichidou, I., Balis, D., Koukouli, M. E., Drosoglou, T., Bais, A., Gratsea, M., Gerasopoulos, E., Liora, N., Poupkou,
1294 A., Giannaros, C. and others: Adverse results of the economic crisis: A study on the emergence of enhanced
1295 formaldehyde (HCHO) levels seen from satellites over Greek urban sites, *Atmos. Res.*, 224, 42–51, 2019.